Doping evolution of the second magnetization peak and magnetic relaxation in (Ba_{1−x}K_{x})Fe_{2}As_{2} single crystals

Yong Liu, Lin Zhou, Kewei Sun, Warren E. Straszheim, Makariy A. Tanatar, Ruslan Prozorov, and Thomas A. Lograsso

Phys. Rev. B **97**, 054511 — Published 16 February 2018

DOI: 10.1103/PhysRevB.97.054511

Doping evolution of second magnetization peak and magnetic relaxation in $(Ba_{1-x}K_x)Fe_2As_2$ single crystals

Yong Liu[1,*] Lin Zhou[1], Kewei Sun[1], Warren E. Straszheim[1], Makariy A. Tanatar[1,2], Ruslan Prozorov[1,2], and Thomas A. Lograsso[1,3]

[1]*Division of Materials Sciences and Engineering, Ames Laboratory, U.S. DOE, Ames, Iowa 50011, USA*

[2]*Department of Physics and Astronomy, Iowa State University, Ames, Iowa 50011, USA*

[3]*Department of Materials Science and Engineering, Iowa State University, Ames, Iowa 50011, USA*

We present a thorough study of doping dependent magnetic hysteresis and relaxation characteristics in single crystals of $(Ba_{1-x}K_x)Fe_2As_2$ ($0.18 \le x \le 1$). The critical current density J_c reaches maximum in the underdoped sample x=0.26 and then decreases in the optimally doped and overdoped samples. Meanwhile, magnetic relaxation rate S rapidly increases and the flux creep activation barrier U_0 sharply decreases in the overdoped sample x=0.70. These results suggest that vortex pinning is very strong in the underdoped regime, but it is greatly reduced in the optimally doped and overdoped regime. Transmission electron microscope (TEM) measurements reveal the existence of dislocations and inclusions in all three studied samples x=0.38, 0.46, and 0.65. An investigation of the paramagnetic Meissner effect (PME) suggests that spatial variations in T_c become small in the samples x=0.43 and 0.46, slightly above the optimal doping levels. Our results support that two types of pinning sources dominate the (Ba_{1-}

* Corresponding author. Email address: yliu@ameslab.gov

$_x$K$_x$)Fe$_2$As$_2$ crystals: (i) Strong δl pinning resulted from the fluctuations in the mean free path l and δT_c pinning from the spatial variations in T_c in the underdoped regime; (ii) Weak δT_c pinning in the optimally doped and overdoped regime.

PACS number(s): 74.70.Xa, 74.25.Wx, 74.25.Sv

I. INTRODUCTION

The studies of vortex dynamics revealed many interesting phenomena in the iron pnictide superconductors. Because of the availability of large and high–quality single crystals, most of researches have been done on 122-type superconductors with $ThCr_2Si_2$ structure. Similar to high T_c cuprate superconductors, a pronounced second magnetization peak (SMP) was observed in magnetization hysteresis loops (MHLs) of $(Ba_{1-x}K_x)Fe_2As_2$ [1-6], $Ba(Fe_{1-x}Co_x)_2As_2$ [3,6,7-13], $BaFe_2(As_{1-x}P_x)_2$ [6,14-15]. One of striking features that that distinguish iron pnictide superconductors from high T_c cuprate superconductors is the observation of strongly disordered vortex structure in iron pnictide superconductors by Bitter decoration [16-22], scanning tunneling microscopy (STM) [23-24], magnetic force microscopy (MFM) [25], small-angle neutron scattering (SANS) measurements [17-18,26-27]. Although long-range ordered vortex lattice (VL) was not observed yet, the so-called Bragg glass may exist, which is a glass but nearly as ordered as a perfect crystal. An ordered vortex structure was observed in an area of 130×50 nm^2 in optimally doped $Ba_{0.6}K_{0.4}Fe_2As_2$ by STM measurement [28]. With a large $Ba_{0.64}K_{0.36}Fe_2As_2$ single crystal, SANS measurement observed Bragg peaks corresponding to a long-range ordered triangular lattice below H=0.75 T. With increasing magnetic field above 0.75 T, diffraction spots smeared and gave the characteristic pattern of circles from a polycrystalline structure, which was interpreted as a vortex order–disorder transition associated with the appearance of SMP in MHLs [29]. In optimally doped $BaFe_2(As_{0.67}P_{0.33})_2$ single crystals, hexagonal VL was formed in the field range from 1 to 16 T revealed by SANS measurement, and no symmetry changes in the VL were observed [30]. In KFe_2As_2 single crystals, a well-ordered hexagonal VL was observed by SANS measurement, with no symmetry transitions up to high fields [31-32].

The disordered VL structure is directly related to a random distribution of pinning potential, implying the pinning mechanisms of iron pnictide superconductors. A pinning potential, U_0, as high as 10^4 K was reported in a $Ba_{0.72}K_{0.28}Fe_2As_2$ single crystal, which was obtained by analyzing the magnetic-field induced broadening of the resistive transition [33]. In a $Ba(Fe_{0.9}Co_{0.1})_2As_2$ single crystal, the scaling of vortex pinning force F_p curves leads to a symmetric peak centered at the reduced field h~0.45, which was interpreted as a result of an inhomogeneous distribution of cobalt ions [8]. Van der Beek *et al*. suggested the existence of two types of pinning sources: (i) Strong pinning resulting from the heterogeneity on the scale of a few dozen to 100 nm; (ii) Weak collective pinning resulting from a disorder at the atomic scale induced by the dopant atoms [34-36]. Through an analysis of the vortex interaction energy and pinning force distributions extracted from Bitter decoration images for $Ba(Fe_{1-x}Co_x)_2As_2$ and $BaFe_2(As_{1-x}P_x)_2$ single crystals, the disordered VL was suggested to be resulted from an inhomogeneous distribution of the dopant atoms on the scale of several dozen to several hundred nanometers [21-22]. Furthermore, it was suggested that the disordered VL is established at a high freezing temperature T_f at $T_f = 0.95T_c$ for $Ba(Fe_{1-x}Co_x)_2As_2$ and $T_f \approx 0.87T_c$ for $BaFe_2(As_{1-x}P_x)_2$ [21-22].

In this study, high-quality single crystals of $(Ba_{1-x}K_x)Fe_2As_2$ were measured as a function of magnetic field H, time t, and temperature T in a wide doping range $0.18 \leq x \leq 1$. We find that the SMP disappears in the samples x=0.43 and 0.46. Furthermore, these samples show reversible magnetization in a broad temperature range for the zero field cooling (ZFC) and field cooling (FC) curves in the temperature-dependent magnetization measurements, whereas the paramagnetic Meissner effect (PME) is observed in other samples. The decay of magnetization nearly follows a power-law time dependence in $(Ba_{1-x}K_x)Fe_2As_2$ single crystals. The logarithmic

dependence of the activation energy U on the critical current J is deduced. We then discuss the possible pinning mechanisms in the samples.

II. Experimental details

The details of growth of $(Ba_{1-x}K_x)Fe_2As_2$ single crystals can be found in Refs. 37 and 38. For magnetization measurements, the large crystals were cut into small plates with typical dimensions of $3 \times 2 \times 0.02$ mm^3 using razor blade. It should be pointed out that the superconducting transition temperature T_c spans several Kelvins for the measured crystals cleaved from one large crystal, which manifests a macro inhomogeneity in the large crystals. Only those crystals showing sharp transition were selected for this study; see Table I and Fig. 1 in Supplemental Material [39]. All the observed features and physical properties are reproducible through the measurements on eighty samples.

Magnetization measurements were performed on Vibrating Sample Magnetometer (VSM) in Physical Property Measurement System (PPMS, Quantum Design). The data were collected after cooling the sample from above T_c to the desired temperature under zero magnetic field or with an application of magnetic field, termed as ZFC and FC, respectively. The MHLs were measured at different temperatures in ZFC procedure. The magnetic field H was applied parallel to the c axis ($H \parallel c$), i.e., perpendicular to the surface of the thin plates. The magnetic field H was ramped at a sweep rate of 1×10^{-3} T/sec between -9 T and $+9$ T.

For magnetic relaxation measurements, the sample was cooled down to the measurement temperature in ZFC procedure. The magnetic field H was then increased to the desired field at a rate of 1×10^{-3} T/sec. After the field was ramped to the desired field, the superconducting coil was changed to persistent mode and the time dependence of magnetization, M vs t curve, was immediately recorded over a period of 1×10^4 seconds.

Temperature dependent magnetization data were recorded in both ZFC and FC procedures. The sample was cooled down to 2 K from above T_c in zero applied magnetic field, and $M(T)$ data were then collected on warming at 1 K/min under an applied field H. The sample was cooled down to 2 K under the same field, and then the FC data were collected on warming at same ramping rate.

The crystal structure analysis by X-ray diffraction can be found in our previous reports [38,40]. Composition of the crystals was determined by using wavelength dispersion x-ray spectroscopy (WDS) of electron microprobe analysis.

Transmission electron microscope (TEM) samples were prepared using an FEI Helios Focused Ion Beam (FIB). TEM characterization was performed on a probe aberration-corrected scanning transmission electron microscope (AC-STEM) (FEI Titan Themis) with a Super-X energy dispersive X-ray spectroscopy (EDS) detector.

III. Results and discussion

A. Second magnetization peak and scaling relation of pinning force density

Figure 1 shows the superconducting transition curves of $(Ba_{1-x}K_x)Fe_2As_2$ (x=0.24, 0.38, 0.43, 0.51, 0.70, and 0.91) single crystals and their MHLs at the reduced temperatures T/T_c~0.9 and 0.75 (sample x=0.91). The sharp superconducting transitions demonstrate that high quality crystals were used in this study. The MHLs of the samples $0.18 \leq x \leq 0.70$ display a rather symmetric shape for the upper (M^+) and lower (M^-) branches, which suggests dominant bulk pinning in these samples [41-42]. All of MHLs exhibit a sharp central peak at around H=0 T. With increasing field, magnetization curves pass through a minimum at a field H_{on}. Above H_{on}, magnetization continuously increases and reaches maximum at a field H_{sp}, so-called SMP named after the low field peak at H=0. With further increasing field, magnetization starts to decrease.

The irreversible magnetization ends at an irreversibility field H_{irr}, where the upper and lower branches of the MHLs merge together with further increasing field. Interestingly, the SMP disappears in the samples x=0.43 and 0.46. It should be pointed out that Song *et al*. had reported doping dependence of critical current density J_c of $(Ba_{1-x}K_x)Fe_2As_2$ single crystals within the doping range $0.23 \leq x \leq 0.52$, which was determined by the MHL measurements [5-6]. In Song *et al*.'s samples, SMP is absent in the doping range $0.36 \leq x \leq 0.50$ [5-6]. The two results are qualitatively consistent with each other. The similar results obtained in two independent works strongly suggest that the absence of SMP is intrinsic phenomenon in $(Ba_{1-x}K_x)Fe_2As_2$ system. We find that the SMP reappears in the MHLs for the samples $0.51 \leq x \leq 0.64$. For the samples in the doping range $0.70 \leq x \leq 0.91$, the SMP is observed at high field region close to H_{irr}. The asymmetric MHLs suggest that the surface pinning and geometrical barrier dominate instead of bulk pinning [41-42]. For the pure KFe_2As_2 sample, there is no SMP observed in the asymmetric MHLs; see Fig. 2 in Supplemental Material [39].

In the underdoped and optimally doped samples $0.18 \leq x \leq 0.38$ and overdoped samples $0.51 \leq x \leq 0.64$, the SMP is featured as a broad peak positioned in the intermediate field away from H_{c2}. It is necessary to distinguish the high field peak observed in the example x=0.70 from the SMP observed in lower doping samples. In conventional superconductors, the SMP is positioned in the vicinity of the upper critical field H_{c2} and the MHLs exhibit a narrow width in a wide field region before the SMP shows up, termed as peak effect (PE); see an example of Nb_3Sn superconductor in Ref. 43. It is generally accepted that PE in conventional superconductors signals a rapid softening of the elastic moduli of the VL as H_{c2} is approached, which in turn can get distorted vortices pinned more strongly by pinning centers and lead to a sharp rise in the critical current [44]. Interestingly, the transformation from SMP to PE was also observed in

$BaFe_2(As_{1-x}P_x)_2$ system with increasing P doping x [6,14].

In order to explore the vortex pinning mechanisms, the critical current density J_c has been calculated from the width of the MHLs using the Bean model $J_c = 20\Delta M/[w(1-w/3l)]$, where ΔM is in unit of emu/cm^3, l is the length and w is the width of the sample (w<l) [45]. Figure 2 shows the double-logarithmic plots of field dependence of J_c for the samples x=0.18, 0.24, 0.28, 0.32, 0.38, 0.43, 0.46, 0.51, 0.64, 0.70, 0.77, and 0.91. For the samples x=0.24, 0.28, 0.32, and 0.38, J_c slightly decreases with increasing field in the low field regime H<0.5 T and exhibits the form of a plateau. With further increasing field, J_c decreases, which can be described by a power-law $J_c \propto H^{-n}$. The power-law dependence terminates at the onset position H_{on} of the SMP. The exponent n varies from 0.44 to 0.63 with increasing doping. Van der Beek *et al*. suggested that J_c in iron pnictides consists of two parts: (i) Strong pinning gives rise to low field peak (the plateau) and power law dependence of $J_c(H)$, which is resulted from the spatial variations of the average dopant atom density on a scale of dozens of nanometers; (ii) Weak collective pinning is field-independent and leads to the formation of SMP, where the dopant atom were treated as points defects [34-36]. For the samples x=0.43 and 0.46, J_c continuously decreases and no SMP is observed. For the samples x=0.51 and 0.64, the SMP reappears. With x exceeding 0.70, the SMP changes to PE. In heavily K doped sample x=0.91, the PE is discernible but very weak. We notice that the exponent n becomes large with increasing doping, up to 0.78 in the sample x=0.91. Starting from the sample x=0.43, the plateau shrinks and it eventually vanishes above x=0.64. These features suggest that vortex pinning is strong in underdoped regime but becomes weak in overdoped regime, which implies different pinning mechanisms in different doping regimes.

The pinning force density F_p is equal to the critical value of the Lorentz force $F_p = J_c \times H$.

There is a maximum F_p^{max} in the plot of F_p vs H. For type II superconductors, it was shown that the normalized pinning force $f = F_p/F_p^{max}$ as a function of reduced field $h = H/H_{c2}$ obeys a scaling relation, i.e. $f = Ah^p(1-h)^q$, where A is prefactor, p and q are the exponents that describe the actual pinning mechanism [46-48]. If single vortex pinning mechanism dominates, the plots of f vs h at different temperatures will fall on a single curve for a given sample. The peak position h as well as the extracted fitting parameters p and q has been used to judge the types of pinning centers in iron pnictide superconductors [1,3,5,6,8,14]. Here, the parameter H_{c2} has been replaced by the irreversibility field H_{irr}. In this study, H_{irr} is defined with the criterion J_c=10 A/cm^2, where the hysteresis width ΔM decreases to a noise level.

Figure 3 shows the plots of the normalized pinning force F_p/F_p^{max} vs the reduced applied magnetic field h=H/H_{irr} for the samples x=0.18, 0.24, 0.38, 0.43, 0.46, 0.51, 0.64, and 0.70. For the sample x=0.18, the peak position gradually shifts from 0.28 at T=6 K to 0.13 at T=9 K. For the sample x=0.24, h values shift from 0.30 at T=22 K to 0.21 at T=25.5 K. It can be seen that h values of the sample x=0.18 show a large shift compared to the sample x=0.24 in the same temperature window ΔT~3 K below T_c. With increasing doping levels, the volume fraction of antiferromagnetic (AFM) ordered phase is supposed to be reduced while the volume fraction of superconducting phase increases in the underdoped regime [49-50]. The samples x=0.18 is therefore characteristic of stronger phase separation, compared to the sample x=0.24. At low temperatures, a part of AFM phase could become weak superconducting regime due to the proximity effect. With increasing temperature or magnetic field, the superconductivity of this area will be suppressed and become normal state. Therefore, the large shift of peak position in the samples x=0.18 should be related to the phase separation. For the optimally doped sample x=0.38, the F_p/F_p^{max} vs h=H/H_{irr} curves overlap well within the temperature window ΔT=2 K

below T_c. A symmetric peak is centered at h= 0.48. Usually, if only one pinning mechanism operates at all temperatures and fields, the pinning force F_p can be scaled on one curve. In a previous study, the peak positions are found at h~0.39, 0.46 and 0.56 for x=0.23, 0.30, and 0.33 in $(Ba_{1-x}K_x)Fe_2As_2$ single crystals, respectively, where the authors defined irreversibility field H_{irr} by a criterion of J_c<100 A/cm^2 [6]. A small H_{irr} will lead to a large $h=H/H_{irr}$ when plotting the scaling relation F_p/F_p^{max} vs $h=H/H_{irr}$. Both studies demonstrate that the peak positions shift from low to high h with increasing doping x.

As shown in Fig. 1(c), the SMP disappears in the sample x=0.43. The MHLs at different temperatures for the samples x=0.43 and 0.46 can be found in Fig. 2 in Supplemental Material [39]. The F_p scaling for the samples x=0.43 and 0.46 is shown in Figs. 3 (d) and (e), respectively. There is one sharp peak at the reduced field h~0.1 (H~0.5 T). As can be seen in Figs. 2 (f) and (g), the field dependence of J_c changes slope at H~0.5-1 T and T=35-36K. Above this field, J_c rapidly decreases, which gives rise to a maximum in the plot of $F_p = J_c \times H$. It is not the normal SMP as we discuss in the other samples. The SMP reappears in the overdoped samples x=0.51. The h values fluctuate between 0.32<h<0.37 in a temperature window ΔT=3 K below T_c. For the samples x=0.64, we can see that the peak shifts towards low h region with increasing temperature. For the sample x=0.70, the PE is observed and h reaches 0.9 at T=12 K. It should be pointed out that a large magnetic relaxation rate is observed in the optimal and overdoped samples, which has a significant influence on the shape of the MHLs. Technically, it is difficult to attain the magnetization very close to t=0. The magnetic relaxation rate increases with increasing temperature. The peak field H_{sp} of the SMPs and irreversibility field H_{irr} are highly affected by the relaxation rate. The scaling of F_p will be not suitable any more. It is a possible explanation on the failure of the F_p scaling for the samples x=0.64 and 0.70.

In Fig. 4(a), J_c are plotted against reduced temperature T/T_c at a fixed field H=0.5 T for all the samples x=0.18, 0.22, 0.24, 0.26, 0.28, 0.32, 0.38, 0.43, 0.46, 0.51, 0.64, 0.70, 0.77, and 0.91. Figure 4(b) shows the doping dependent J_c at T/T_c=0.20, 0.52 and 0.80. It can be seen that J_c reach maximum at around x=0.26. This doping is exactly located at the boundary of two doping regimes in $(Ba_{1-x}K_x)Fe_2As_2$ phase diagram, where AFM transition line coupled with tetragonal to orthorhombic structure transition terminates [49-50]. The similar feature had been observed in $Ba(Fe_{1-x}Co_x)_2As_2$, where the presence of fine orthorhombic structure domains leads to the J_c maximum [10]. The orthorhombic structure domains have been directly observed in the parent compounds and underdoped samples by using polarized light microscopy [10,51-53]. In the previous studies on $(Ba_{1-x}K_x)Fe_2As_2$, high J_c were observed between $0.25 \leq x \leq 0.30$, and J_c exceed 10^5A/cm^2 at T=25K and H=6 T for x=0.30 [5-6]. To identify the origin of strong pinning at the boundary is the key to understand the pinning mechanisms and formation of SMP in $(Ba_{1-x}K_x)Fe_2As_2$ single crystals.

B. Microstructural features

The relation between microstructures, the properties of the VL, and critical currents has been the heart of the matter on the study of vortex dynamics [46-48]. The defects in the crystals are thought to have a strong influence on the pinning behavior and the shape of the magnetization curve. Compared to the intensive studies on the magnetic properties, only a few works have been done on the microstructures of iron pnictide superconductors. The structure domains in the parent compounds AFe_2As_2 (A=Sr and Ca) had been analyzed by TEM from room temperature down to 20 K [54]. High-resolution transmission electron microscopy (HRTEM) analysis of a $Ba_{0.72}K_{0.28}Fe_2As_2$ crystal indicates no noticeable crystal defects that can act as pinning centers [33]. Defects with a size of 5–10 nm, possibly secondary phase precipitates, were

observed in single crystalline $PrFeAsO_{1-y}$ [34]. It was found that $Ba(Fe_{1-x}Co_x)_2As_2$ thin films can accept a very high density of pins (15–20 vol%) without T_c suppression [55]. The vertically aligned, self-assembled pins were clarified as $BaFeO_2$ nanorods and nanoparticles in a diameter of 4–5 nm. The oxygen could be introduced when synthesizing the targets [55]. In order to clarify the pinning sources in $(Ba_{1-x}K_x)Fe_2As_2$ single crystals, we performed TEM measurements on the samples x=0.38, 0.43, 0.46 and 0.65.

Figure 5 shows TEM results of sample x=0.38, which is characteristic of the SMP. Figure 5(a) shows dislocations in a low-magnification TEM image taken along the [001] zone axis. Observation was also performed perpendicular to the c axis. Figure 5(b) shows some needle-like inclusions observed along the [100] zone axis. This needle-like inclusion is nearly 500 nm long perpendicular to the c axis and ~15nm thick along the c axis. The light area at the end of the needle-like inclusion is grown coherently with the matrix, as shown in Figs. 5(c) and (d). EDS analysis reveals the inclusion is FeAs rich with less Ba and K elements compared to the matrix. The formation of the inclusion can be explained by the fast growth of crystals during the cooling process such that some flux materials were still kept in the crystals. Figures 5(e) and (f) show high resolution high-angle-annular-dark-field (HAADF) scanning transmission electron microscopy (STEM) images of sample x=0.38 along [001] and [100] zone axis. The B/K and FeAs layers are clearly discerned and no visible defects are found at the atomic level.

Figure 6(a) shows dislocations observed in the sample x=0.46. Needle-like inclusion is also observed in this sample, as shown in Fig. 6(b). However, the length of the needle-like inclusion is ~30 nm, which is much shorter than that observed in the sample x=0.38. Figure 6(c) shows HR-STEM image of sample x=0.46 along [100] zone axis. The uniform contrast in the Ba/K atomic sites indicates a uniform mixing of Ba and K without ordering. The similar feature is also

observed in the sample x=0.43; see Fig. 3 in the Supplemental Material [39]. Figure 6(d) shows the selected area electron diffraction (SAED) pattern along [100] zone axis. There are no superlattice diffraction spots observed in the SAED pattern, which further proves that Ba and K elements do not form ordered structure. Figures 6(e) and (f) shows HR-STEM image of sample x=0.65 along [100] zone axis. Again, the needle-like inclusion is observed, as shown in Fig. 6(f). As a result, this sparse extended defect may contribute little to the formation of SMP, but dense defects could work.

C. Magnetic relaxation

Dynamic properties of the flux motion are investigated through the magnetic relaxation measurements on $(Ba_{1-x}K_x)Fe_2As_2$ (x=0.24, 0.32, 0.43, 0.62 and 0.70) single crystals. In Figs. 7(a) and (b), we show the double-logarithmic plots of $|M|$ vs t at different fields and at T=20 K for the sample x=0.24. As can be seen, $\ln|M|$ nearly follows a linear dependence on $\ln t$ after the first 1×10^2 seconds. Figure 7(c) shows the MHL together with the magnetic relaxation data shown in Figs. 7(a) and (b), both measured at T=20 K. One can see that the SMP shifts from 2.7 T to 2 T after 1×10^4 seconds. The relaxation rate S has been defined as the logarithmic time derivative of the magnetization $S = -d\ln|M|/d\ln t$ [56]. It is found that S shows a minimum at S_{min}=1.5 T. At H=9 T, the magnetization rapidly relaxes to its equilibrium value. Figure 7(d) shows the plots of $-T\ln|dM/dt|$ against M, which equals the plots of activation energy U vs J relation. The slope of the curves changes at H=2 T. The analysis of field dependent relaxation data indicates a crossover of relaxation dynamics with increasing field across the SMP.

The similar results had been reported in $YBa_2Cu_3O_{7-\delta}$ [57], $Ba(Fe_{0.93}Co_{0.07})_2As_2$ [9], and $Ba_{0.72}K_{0.28}Fe_2As_2$ [4], which had been interpreted as a crossover from elastic to plastic creep [4,9,57]. In the field range $H<H_{sp}$, the vortex pinning is mainly determined by the collective

pinning resulted from weak point defects. The activation energy U increases with field for elastic creep, while it decreases with field for plastic creep. The creep is governed by the mechanism that has a lower potential. As field exceeds H_{sp}, the plastic creep dominates and vortices are primarily pinned by extended defects such as dislocations [57,58]. Interestingly, the relaxation rate $S(H)$ are featureless over the field range associated with the SMP in $BaFe_{1.82}Ni_{0.18}As_2$ with T_c=8 K [59]. It should be pointed out that the SMP was observed at temperatures below $T_c/2$ and vanished at higher temperatures in an inhomogeneous $Ba_{0.75}K_{0.25}Fe_2As_2$ single crystal, where T_c ranges from 22 to 28 K [60]. It was found that the crossover from collective to plastic pinning observed in the SMP disappears above 12 K with plastic pinning replacing collective pinning [60]. In this study, the sample x=0.24 shows T_c at 26.6 K and the SMP is clearly seen up to T=24 K; see Fig. 2(c) in Supplemental Material [39].

Figure 8(a) shows the magnetic relaxation data collected at different temperatures and at H=0.5 T. The relaxation rate S was calculated and shown in Fig. 8(b). One can see that S does not show a monotonic change with varying temperature. It reaches a maximum at around T=10 K, and then decreases with further increasing temperature. The broad peak in $S(T)$ curve was also observed in $Ba(Fe_{1-x}Co_x)_2As_2$ single crystals [9,12].

It is well know that the logarithmic decay of magnetic relaxation can be interpreted within the framework of the Anderson-Kim flux creep model, where the activation energy U is linearly dependent on current density J [56,61] For the non-logarithmic decay observed in high T_c superconductors, the collective pinning theory was proposed. Feigel'man *et al.* [62-63] considered collective pinning by weak disorder caused by a random distribution of weak defects and showed that the activation energy exhibits a power law dependence on the current density,

$$U(J) = U_0(J_c/J)^{\mu}. \quad (1)$$

Equation (1) was often modified into its interpolation form

$$U(J) = U_0[(J_c/J)^{\mu} - 1]. \quad (2)$$

The magnetization decay was described by the interpolation formula [62,64-65],

$$J(T,t) = J_c\left[1 + \frac{\mu kT}{U_0}\ln\left(\frac{t}{t_0}\right)\right]^{-1/\mu}, \quad (3)$$

where J_c is the critical current density at which the flux creep activation barrier U vanishes, and t_0 is a microscopic time scale. In the collective creep model the exponent μ depends on the dimensionality of the system and the field and current regime. For the three-dimensional case, at low temperatures and moderate magnetic fields but relatively high currents, single vortex creep is described with μ=1/7. In the single vortex creep limit, i.e. $\mu \rightarrow 0$, the magnetization decay can be described by the power law [66]

$$J(t) = J_c\,(t/t_0)^{-T/U_0}. \quad (4)$$

By assuming the creep activation barrier U grows logarithmically with decreasing current J

$$U(J) = U_0\ln(J_c/J), \quad (5)$$

Vinokur *et al*. proposed an exact solution describing flux creep in high T_c superconductors and predicted that $\ln M(t)$ exhibits a linear dependence upon $\ln t$ [66]. The logarithmic J dependence provides a good approximation for the creep activation barrier in the single-vortex creep regime.

Since we observed that the magnetization M follows the power law dependence on time t, it is expected that $U(J)$ also follows Eq. (5) in $(Ba_{1-x}K_x)Fe_2As_2$ single crystals. The method proposed by Maley *et al*. [67] was frequently used to determine the form of the temperature dependence of the activation energy U. Briefly, magnetic relaxation in superconductors is based on an Arrhenius rate equation $dM/dt \propto \exp(-U/k_BT)$, where U is effective activation energy. A rearrangement leads to

$$U = -k_BT\left[\ln\left(\frac{dM}{dt}\right) - C\right]. \quad (6)$$

Here C is a temperature-independent constant, which is used as a fitting parameter. The determination of parameter C requires that U is a continuous and smooth function of J. Since M is proportional to the superconducting current density, J, the activation energy U is usually plotted in the form of U vs M. For the sample x=0.24, the parameter C=40 yields a continuous and smooth curve, as shown in Fig. 8(c). In the previous studies, the parameters C=40, 27, and 14 had been used in $Ba_{0.75}K_{0.25}Fe_2As_2$ [60], $Ba_{0.72}K_{0.28}Fe_2As_2$ [4] and $BaFe_{1.82}Ni_{0.18}As_2$ [59] single crystals, respectively. In order to get the smooth $U(M)$ curves, the activation energy U had been modified by using a scaling function $g(T/T_c) = [1-(T/T_c)^{1.5}]$ [4,59,60]. In this work, the parameter C=40 works well and all the segments collected within a broad temperature range can collapse into one single curve. As shown in Fig. 8(c), $U(J)$ relation can be well described by Eq. (5). In an early report, Konczykowski *et al*. found that the $U(J)$ relation in their $Ba_{0.6}K_{0.4}Fe_2As_2$ single crystals follows Eq. (1) with μ~0.8 [68].

Figures 9(a) and (b) show the MHLs together with relaxation data obtained in the sample x=0.32 at T=20 K and 33 K, respectively. In Fig. 9(a), MHL shows an onset peak at H_{on}, where the magnetization passes through the minimum and rapidly increases. This onset peak shifts towards low field region and vanishes with increasing temperature. It already disappears in the MHL measured at T=33 K; see Fig. 9(b). With increasing field, the relaxation rate S monotonously reduces but shows a kink at the field close to H_{on}. At T=33 K, the relaxation rate S passes through a minimum at H=2 T and rapidly increases, similar to those observed in the sample x=0.24. The multiple magnetization peak feature is observed in the optimally doped samples $0.32 \leq x \leq 0.38$ and becomes more pronounced in the overdoped samples $0.51 \leq x \leq 0.70$. Remember that the SMP disappears in the samples x=0.43 and 0.46. The observation of multiple magnetization peaks was first reported by Shen *et al*. in a $Ba_{0.6}K_{0.4}Fe_2As_2$ single crystal

[69]. It should be pointed out that the onset peak was observed and well characterized in detwinned $YBa_2Cu_3O_{7-\delta}$ crystals, which was ascribed to a disorder-induced transition from a relatively ordered Bragg glass to a highly disordered vortex glass [70-72].

Figure 9(c) shows the temperature dependence of S at a fixed field H=0.5 T. Again, one can see that S increases first and reach a maximum at T=12 K. Figure 9(d) shows the logarithmically dependent $U(J)$ relation described by the Eq. (5). For the sample x=0.32, the application of parameter C=40 also yields a smooth $U(J)$ curve.

Figure 10(a) shows the double-logarithmic plots of time dependence of magnetization for the sample x=0.43 collected at different temperatures with a fixed field H=0.5 T. With increasing temperature approaching T_c=38.4 K, the magnetization relaxes to its equilibrium value within a narrow time window. At T=32 K, the magnetization almost approaches its equilibrium value after 4×10^3 seconds. At T=34 K, the $M(t)$ curve becomes flat after ~300 seconds. For the field dependent relaxation shown Fig. 10(b), the magnetization rapidly decreases to its equilibrium value above H=1.5 T as the data were collected even at T=20 K, far below T_c=38.4 K. There is a kink observed in $M(t)$ curves for some mediate fields $1.5<H<3$ T, indicated by a black arrow in Fig. 10(b). Above H=3.5 T, the magnetization signal becomes unstable after 1×10^3 seconds. One possible explanation on the origin of the kink could be the thermal instability of magnetic relaxation in the sample because of very weak vortex pinning. A large bundle of vortices depin and are expelled out of the sample. Figures 10(c) shows a monotonic change and rapid increase of S with increasing field before H=3 T. Above H=3.5 T, the magnetization rapidly relaxes to its equilibrium value and displays noise-like signal. Therefore we calculate the relaxation rate within the time window before the magnetization drops to the equilibrium value. The large S values, $S>0.1$, were obtained and plotted in Fig. 10(c). The peak at H=4 T should not take any

physical explanation because S values were calculated within the different time windows. The temperature dependence of S at H=0.5 T is shown in Fig. 10(d). One can see that S still shows a peak between 5<T<15 K and then increases quickly above T=20 K. In the samples x=0.24 and 0.32, the peak ranges from 3 K to the temperature close to T_c. The fast relaxation in the sample x=0.43 above T=20 K suggests weak vortex pinning, consistent with the absence of the SMP. The dramatic change of $S(T)$ shape suggests that the formation of $S(T)$ peak is related to the strong vortex pinning. Figure 10(e) shows the activation energy U also follows a logarithmic dependence on critical current J. All the segments collapse into single curve by choosing parameter C=36, which is slightly smaller than 40 applied to the sample x=0.24 and 0.32.

Figure 11(a) shows the double-logarithmic plots of time dependence of magnetization for the sample x=0.62 with T_c=25.8 K collected at different fields with a fixed temperature T=19 K. The magnetic relaxation data collected at different temperatures with a fixed field H=0.5 T are shown in Fig. 10(b). Figure 11(c) shows the MHL measured at T=19 K together with the relaxation data shown in Fig. 11(a). As can be seen in Fig. 11(c), the magnetization almost drops to its equilibrium value after 1×10^4 seconds; see Fig. 7(c) for a comparison. Figure 11(c) also clearly reveals that the relaxation has a significant influence on the shape of MHLs for the overdoped samples. Although the two samples x=0.24 and 0.62 have the similar T_c (see Table I), a large relaxation rate S is observed in the sample x=0.62. The underdoped samples have much stronger vortex pinning while the overdoped samples are characteristic of weak vortex pinning. Figure 11(d) shows the temperature dependence of relaxation rate for the sample x=0.62. Similar to the sample x=0.43, the relaxation rate S rapidly increases at a temperature far below T_c, ~16 K. Figure 11(e) shows $U(J)$ relation on a logarithmic dependence. The parameter C=8 is chosen to set all segments into one smooth curve, which is significantly smaller than the previous values.

Figure 12(a) shows the time dependence of magnetization for the sample x=0.70 with T_c=18.3 K collected at different temperatures with a fixed field H=0.5 T. With increasing temperature, the magnetization relaxes to its equilibrium value within a narrow time window, as indicated by the arrow in Fig. 12(a). Above T=5 K, relaxation rate S already reaches ~0.2, as shown in Fig. 12(b). Figure 12(c) shows the $U(J)$ relation on a logarithmic dependence, where the parameter C=8 is applied to set all segments into one smooth curve. Because very large relaxation happens above 10 K, only three segments below 8 K are reliable for the analysis.

In Table II we summarize the fitting parameters by applying Eq. (5) to the current density J (presented by the magnetization M) dependence of the activation energy U for $(Ba_{1-x}K_x)Fe_2As_2$ (x=0.24, 0.32, 0.43, 0.62 and 0.70) single crystals. Figure 13 shows the doping dependent relaxation rate S and activation barrier U_0 at H=0.5 T. As can be seen in Table II and Fig. 13, the vortex pinning in the underdoped regime is very strong, which gives rise to large activation barrier U_0 and small relaxation rate S. In overdoped regime, activation barrier U_0 is greatly reduced while relaxation rate S rapidly increases above x=0.70. Vortex pinning becomes very weak. The C parameter shows the similar doing dependence as U_0 and J_c behave in Table II. Obviously, the C parameter is also related to the strength of vortex pinning.

D. Paramagnetic Meissner effect

Figure 14 shows the temperature dependence of magnetization for the samples x=0.24, 0.32, 0.43, and 0.64. The FC data are flat curves, while ZFC curves bend down to low temperatures. The insets show the superconducting transition curves in the vicinity of T_c. One can see that ZFC and FC curves show reversible magnetization in a narrow temperature window below T_c for the samples x=0.24, 0.32, and 0.64. With further cooling, ZFC and FC curves separate at a temperature T_{irr}. The FC curves then rise and form a dip. Below the dip temperature, the

magnetization even exceeds the paramagnetic background above T_c. Interestingly, sample x=0.43 shows a very different behavior. At low field H=0.5 T, one can see a dip. With increasing field, the dip becomes invisible. And ZFC and FC curves show a broad temperature range of reversible magnetization below T_c, which implies a broad vortex liquid regime in the vortex phase diagram. Both the absence of the SMP and the wide reversible magnetization suggest a weak pinning in the sample x=0.43. Salem-Sugui *et al*. had reported the temperature dependence of magnetization at different fields in $(Ba_{1-x}K_x)Fe_2As_2$ (x=0.28 and 0.25) single crystals under ZFC and FC modes [73]. One may notice that the reversible magnetization below T_c is in a quite narrow temperature window. Most importantly, the FC data always show a dip right below T_c [73]. When one looks over previous results, similar feature was also observed in $BaFe_{2-x}Co_xAs_2$ (x=0.19) [26].

In small size superconductors and ceramic superconductors, a paramagnetic response or paramagnetic Meissner effect (PME) was observed [74]. For small size superconductors, the compression of the flux trapped inside the giant vortex state can result in the PME [75-77]. The PME was also observed in $YBa_2Cu_3O_{7-\delta}$ [78-81] and $La_{1.85}Sr_{0.15}CuO_4$ [82] single crystals. The magnitude of supercurrents flowing in the critical state largely depends on the magnetic fields, temperature, and sample-specific pinning characteristics. One important parameter which also determines the field and current distributions in the FC critical state is the cooling rate. It was demonstrated that one may change the high-field response of the superconductor from diamagnetic to paramagnetic by varying the cooling rate [78-82]. The PME can be understood as the unusual influence of pinning on the FC magnetization caused by the inhomogeneous cooling and subsequent flux compression in a large crystal, mostly due to its size. In Fig. 15, we show the effect of cooling rate on the dip for the sample x=0.32. With applying the fast cooling rate at 10 K/min and slow cooling rate at 1 K/min, the dip shifts ~0.2 K toward the low temperature

regime. Interestingly, fast cooling leads to a more pronounced jump, which supports that inhomogeneous cooling may be responsible for the PME effect in the samples. It is suggested that the granularity in iron pnictide superconductors close to T_c should be responsible for PME [83]. One may recall that the analysis of the vortex interaction energy and pinning force distributions for $Ba(Fe_{1-x}Co_x)_2As_2$ and $BaFe_2(As_{1-x}P_x)_2$ single crystals revealed that the disordered VL should be resulted from strong pinning due to spatial fluctuations of T_c and it is established at a high freezing temperature T_f close to T_c [21-22]. As the sample is cooled down in FC procedure, the screening currents are, at temperatures immediately below T_c, restricted to the intragranular contribution, a situation that remains until the temperature reaches T_{dip}. Below T_{dip}, the intergranular currents might contribute with a signal that can be either paramagnetic or diamagnetic [83].

E. Pinning mechanisms

Our systematic investigations on the magnetization with varying doping x, magnetic field H, temperature T, and time t provide a comprehensive scenario of vortex pinning in $(Ba_{1-x}K_x)Fe_2As_2$ superconductors. As we already demonstrate, J_c reaches maximum at x=0.26, where AFM transition line coupled with tetragonal to orthorhombic structure transition terminates in the phase diagram [49-50]. The pronounced plateau in the plots of J_c vs H is observed in the underdoped samples, as shown in Fig. 2. Ishida *et al*. had studied doping-dependent J_c in K, Co, and P-doped $BaFe_2As_2$ single crystals [6]. All three systems exhibit maximum J_c at around the critical doping point where AFM transition line terminates and orthorhombic structure disappears. A quantitative analysis of the T–dependent J_c indicates that the two pinning mechanisms, namely, the spatial variations in T_c (referred to as δT_c pinning) and the fluctuations in the mean free path (δl pinning), are enhanced in the underdoped regime, which gives rise to

the maximum J_c [6].

As far as pinning sources are concerned, the formation of structural domains in the orthorhombic phase has been well studied both in $Ba(Fe_{1-x}Co_x)_2As_2$ and $(Ba_{1-x}K_x)Fe_2As_2$ by using polarized light microscopy [10,51-53]. The domain walls extend throughout the samples and act as the extended pinning centers. With the increasing doping x, domain structure becomes more intertwined and fine due to a decrease of the orthorhombic distortion [10]. On the other hand, the coexistence of AFM ordered phase and superconducting phase on a scale of dozens of nanometers was revealed in a slightly underdoped $(Ba_{1-x}K_x)Fe_2As_2$ single crystal with T_c of 32 K [84]. The muon spin rotation (μSR) and infrared spectroscopy experiments demonstrated that bulk magnetism and superconductivity coexist and compete on the nanometer length scale in underdoped $(Ba_{1-x}K_x)Fe_2As_2$ [85] and $BaFe_{1.89}Co_{0.11}As_2$ [86]. The dopant clusters on the scale of a few nanometers were directly observed in $Ba_{0.72}K_{0.28}Fe_2As_2$ crystals by atom probe tomography technique [87]. Either coexistence of superconductivity and magnetism on a nanoscale or structure domains will result in limiting the mean free path l and cause strong δl pinning. Ishida *et al*. also pointed out that the spatial variations in T_c can be expressed as $\Delta T_c = |dT_c/dx|\Delta x$, where dT_c/dx is the slope of the $T_c(x)$ curve and Δx is its spatial variation in x [6]. In the T_c□x phase diagram T_c rapidly increases in the underdoped regime. The δT_c pinning is also expected to increase in the underdoped regime. Therefore both δl and δT_c pinnings are enhanced and leads to maximum J_c in the sample x=0.26.

We find that the SMP is absent within a narrow doping range $0.4<x<0.5$ in our $(Ba_{1-x}K_x)Fe_2As_2$ single crystals. Furthermore, these samples do not show PME, which implies weak T_c fluctuations. With doping exceeding x=0.51, the SMP reappears. In the optimally doped regime, the contribution from δl pinning rapidly decreases and the δT_c pinning is comparable to the δl

pinning [6]. It should be pointed out that $(Ba_{1-x}K_x)Fe_2As_2$ phase diagram exhibits a plateau in the optimally doped and slightly overdoped regime $0.32 \leq x \leq 0.46$, where dT_c/dx is relatively small. Therefore, T_c fluctuations become small and weak δT_c pinning is expected within this doping range, leading to the absence of the SMP. With further increasing doping levels, T_c gradually decreases while dT_c/dx becomes large. The δT_c pinning may increase and result in the reappearance of the SMP in the overdoped regime. This picture is consistent with the absence of PME in the samples x=0.43 and 0.46. Sundar *et al*. had measured MHLs in an inhomogeneous $Ba_{0.75}K_{0.25}Fe_2As_2$ single crystal with T_c=28 K but very broad transition [60]. The SMP had been observed at low temperatures but vanished at higher temperatures. They found that the crossover from collective to plastic pinning observed in the SMP disappears above 12 K with plastic pinning replacing collective pinning [60]. In such inhomogeneous crystals, the SMPs are broad. With increasing temperature, more and more low-T_c superconducting area will contribute to flux pinning. The SMPs are supposed to become broader. Finally, the SMP "disappears" at certain temperature. The peak fields display a continuous change when sweeping the magnetic field. Because the peak field ranges from low-field to high-field region, the plastic pinning is certainly observed within the whole field range. It should be emphasized that, in our case, weak δT_c pinning (small T_c variations) should be responsible for the disappearance of the SMP.

Finally, we would like to mention recently discovered line compounds $CaAFe_4As_4$ (A=K, Rb, Cs) and $SrAFe_4As_4$ (A=Rb, Cs), where alkaline earth metal and alkali metal layers are inserted alternately between the Fe_2As_2 layers along c-axis direction [88]. In $(Ba_{1-x}K_x)Fe_2As_2$ system, our TEM measurements indicate no evidence that Ba and K elements form ordered layer structure and alternate along c axis at around x=0.50. The disappearance of the SMP in the samples x=0.43 and 0.46 cannot be ascribed to an ordered structure.

IV. CONCLUSIONS

We have systematically studied the doping evolution of the SMP, current density J_c, magnetization relaxation in $(Ba_{1-x}K_x)Fe_2As_2$ superconductors. We find that J_c reach maximum at x=0.26 at a fixed field H=0.5 T, where AFM transition line terminates in the phase diagram. Two types of pinning sources most probably contribute to the vortex pinning. Either structure domains or coexistence of superconductivity and magnetism on a nanoscale should act as pinning centers and lead to strong δl pinning in the underdoped regime. On the other hand, the spatial fluctuations of dopant atoms provide a background pinning as point defects ranging from underdoped to overdoped regime. The δT_c pinning is enhanced in the underdoped regime but becomes weak in the samples x=0.43 and 0.46, where the SMP disappears. With x exceeding 0.50, δT_c pinning may enhance again and the SMP reappears. This picture is supported by analyzing PME in the crystals, which suggests small T_c fluctuations in the samples x=0.43 and 0.46.

We find that the magnetic relaxation nearly follows the power-law time dependence and the activation energy U can be described by the logarithmic dependence on critical density J. We demonstrate that the vortex pinning in the underdoped regime is very strong, which gives rise to large activation barrier U_0 and small relaxation rate S. With increasing doping levels, vortex pinning becomes weak in the overdoped regime. Activation barrier U_0 is greatly reduced while relaxation rate S rapidly increases above x=0.70.

ACKNOWLEDGMENTS

This work was supported by the U.S. Department of Energy (DOE), Office of Science,

Basic Energy Sciences, Materials Science and Engineering Division. The research was performed at Ames Laboratory, which is operated for the U.S. DOE by Iowa State University under contract # DE-AC02-07CH11358.

References

1. H. Yang, H. Luo, Z. Wang, and H.-H. Wen, Appl. Phys. Lett. **93**, 142506 (2008).
2. H.-J. Kim, Y. Liu, Y. S. Oh, S. Khim, I. Kim, G. R. Stewart, and K. H. Kim, Phys. Rev. B **79**, 014514 (2009).
3. D. L. Sun, Y. Liu, and C. T. Lin, Phys. Rev. B **80**, 144515 (2009).
4. S. Salem-Sugui, Jr., L. Ghivelder, A. D. Alvarenga, L. F. Cohen, K. A. Yates, K. Morrison, J. L. Pimentel, Jr., H. Luo, Z. Wang, and H.-H. Wen, Phys. Rev. B **82**, 054513 (2010).
5. D. Song, S. Ishida, A. Iyo, M. Nakajima, J.-I. Shimoyama, M. Eisterer, and H. Eisaki, Sci. Rep. **6**, 26671 (2016).
6. S. Ishida, D. Song, H. Ogino, A. Iyo, H. Eisaki, M. Nakajima, J.-I. Shimoyama, and M. Eisterer, Phys. Rev. B **95**, 014517 (2017).
7. Y. Nakajima, T. Taen, and T. Tamegai, J. Phys. Soc. Jpn. **78**, 023702 (2009).
8. A. Yamamoto, J. Jaroszynski, C. Tarantini, L. Balicas, J. Jiang, A. Gurevich, D. C. Larbalestier, R. Jin, A. S. Sefat, M. A. McGuire, B. C. Sales, D. K. Christen, and D. Mandrus, Appl. Phys. Lett. **94**, 062511 (2009).
9. R. Prozorov, N. Ni, M. A. Tanatar, V. G. Kogan, R. T. Gordon, C. Martin, E. C. Blomberg, P. Prommapan, J. Q. Yan, S. L. Bud'ko, and P. C. Canfield, Phys. Rev. B **78**, 224506 (2008).
10. R. Prozorov, M. A. Tanatar, N. Ni, A. Kreyssig, S. Nandi, S. L. Bud'ko, A. I. Goldman, and P. C. Canfield, Phys. Rev. B **80**, 174517 (2009).
11. R. Prozorov, M. A. Tanatar, E. C. Blomberg, P. Prommapan, R. T. Gordon, N. Ni, S. L. Bud'ko, and P. C. Canfield, Physica C **469**, 667 (2009).
12. B. Shen, P. Cheng, Z. Wang, L. Fang, C. Ren, L. Shan, and H.-H. Wen, Phys. Rev. B **81**, 014503 (2010).
13. R. Kopeliansky, A. Shaulov, B. Ya. Shapiro, Y. Yeshurun, B. Rosenstein, J. J. Tu, L. J. Li, G. H. Cao, and Z. A. Xu, Phys. Rev. B **81**, 092504 (2010).

14. L. Fang, Y. Jia, J. A. Schlueter, A. Kayani, Z. L. Xiao, H. Claus, U. Welp, A. E. Koshelev, G. W. Crabtree, and W.-K. Kwok, Phys. Rev. B **84**, 140504(R) (2011).
15. S. Salem-Sugui, Jr., J. Mosqueira, A. D. Alvarenga, D. Sóñora, E. P. Herculano, D. Hu, G. Chen, and H. Luo, Supercond. Sci. Technol. **28**, 055017 (2015).
16. L. Ya. Vinnikov, T. M. Artemova, I. S. Veshchunov, N. D. Zhigadlo, J. Karpinski, P. Popovich, D. L. Sun, C. T. Lin, A. V. Boris, JETP Letters **90**, 299 (2009).
17. M. R. Eskildsen, L. Ya. Vinnikov, T. D. Blasius, I. S. Veshchunov, T. M. Artemova, J. M. Densmore, C. D. Dewhurst, N. Ni, A. Kreyssig, S. L. Bud'ko, P. C. Canfield, and A. I. Goldman, Phys. Rev. B **79**, 100501(R) (2009).
18. M. R. Eskildsen, L.Ya. Vinnikov, I. S. Veshchunov, T. M. Artemova, T. D. Blasius, J. M. Densmore, C. D. Dewhurst, N. Ni, A. Kreyssig, S. L. Bud'ko, P. C. Canfield, A. I. Goldman, Physica C **469**, 529 (2009).
19. L. Ya. Vinnikov, A. G. Troshina, I. S. Veschunov, D. Analytis, I. R. Fisher, Y. Liu, C. T. Lin, L. Fang, U. Welp, and W. K. Kwok, JETP Letters **96**, 655 (2013).
20. L. Vinnikov, A. Friedman, I. Felner, A. Troshina, and Y. Yeshurun, J. Phys.: Conf. Ser. **507**, 012013 (2014).
21. S. Demirdiş, C. J. van der Beek, Y. Fasano, N. R. Cejas Bolecek, H. Pastoriza, D. Colson, and F. Rullier-Albenque, Phys. Rev. B **84**, 094517 (2011).
22. S. Demirdiş, Y. Fasano, S. Kasahara, T. Terashima, T. Shibauchi, Y. Matsuda, Marcin Konczykowski, H. Pastoriza, and C. J. van der Beek, Phys. Rev. B **87**, 094506 (2013).
23. Y. Yin, M. Zech, T. L. Williams, X. F. Wang, G. Wu, X. H. Chen, and J. E. Hoffman, Phys. Rev. Lett. **102**, 097002 (2009).
24. C.-L. Song, Y. Yin, M. Zech, T. Williams, M. M. Yee, G.-F. Chen, J.-L. Luo, N.-L. Wang, E. W. Hudson, and J. E. Hoffman, Phys. Rev. B **87**, 214519 (2013).
25. H. Yang, B. Shen, Z. Wang, L. Shan, C. Ren, and H.-H. Wen, Phys. Rev. B **85**, 014524

(2012).

26. D. S. Inosov, T. Shapoval, V. Neu, U. Wolff, J. S. White, S. Haindl, J. T. Park, D. L. Sun, C. T. Lin, E. M. Forgan, M. S. Viazovska, J. H. Kim, M. Laver, K. Nenkov, O. Khvostikova, S. Kühnemann, and V. Hinkov, Phys. Rev. B **81**, 014513 (2010).
27. P. Das, T. O'Brien, M. Laver, C. D. Dewhurst, N. Ni, S. L. Bud'ko, P. C. Canfield, and M. R. Eskildsen, Supercond. Sci. Technol. **23**, 054007 (2010).
28. L. Shan, Y.-L. Wang, B. Shen, B. Zeng, Y. Huang, A. Li, D. Wang, H. Yang, C. Ren, Q.-H. Wang, S. H. Pan, and H.-H. Wen, Nat. Phys. **7**, 325 (2011).
29. S. Demirdiş, C. J. van der Beek, S. Mühlbauer, Y. Su, and Th Wolf, J. Phys.: Condens. Matter **28**, 425701 (2016).
30. R. Morisaki-Ishii, H. Kawano-Furukawa, A. S. Cameron, L. Lemberger, E. Blackburn, A. T. Holmes, E. M. Forgan, L. M. DeBeer-Schmitt, K. Littrell, M. Nakajima, K. Kihou, C. H. Lee, A. Iyo, H. Eisaki, S. Uchida, J. S. White, C. D. Dewhurst, J. L. Gavilano, and M. Zolliker, Phys. Rev. B **90**, 125116 (2014).
31. H. Kawano-Furukawa, C. J. Bowell, J. S. White, R. W. Heslop, A. S. Cameron, E. M. Forgan, K. Kihou, C. H. Lee, A. Iyo, H. Eisaki, T. Saito, H. Fukazawa, Y. Kohori, R. Cubitt, C. D. Dewhurst, J. L. Gavilano, and M. Zolliker, Phys. Rev. B **84**, 024507 (2011).
32. H. Kawano-Furukawa, Lisa DeBeer-Schmitt, H. Kikuchi, A. S. Cameron, A. T. Holmes, R. W. Heslop, E. M. Forgan, J. S. White, K. Kihou, C. H. Lee, A. Iyo, H. Eisaki, T. Saito, H. Fukazawa, Y. Kohori, and J. L. Gavilano, Phys. Rev. B **88**, 134524 (2013).
33. X.-L. Wang, S. R. Ghorbani, S.-I. Lee, S. X. Dou, C. T. Lin, T. H. Johansen, K.-H. Müller, Z. X. Cheng, G. Peleckis, M. Shabazi, A. J. Qviller, V. V. Yurchenko, G. L. Sun, and D. L. Sun, Phys. Rev. B **82**, 024525 (2010).
34. C. J. van der Beek, G. Rizza, M. Konczykowski, P. Fertey, I. Monnet, Thierry Klein, R. Okazaki, M. Ishikado, H. Kito, A. Iyo, H. Eisaki, S. Shamoto, M. E. Tillman, S. L. Bud'ko, P.

C. Canfield, T. Shibauchi, and Y. Matsuda, Phys. Rev. B **81**, 174517 (2010).

35. C. J. van der Beek, M. Konczykowski, S. Kasahara, T. Terashima, R. Okazaki, T. Shibauchi, and Y. Matsuda, Phys. Rev. Lett. **105**, 267002 (2010).
36. C. J. van der Beek, S. Demirdis, M. Konczykowski, Y. Fasano, N. R. Cejas Bolecek, H. Pastoriza, D. Colson, F. Rullier-Albenque, Physica B: Condensed Matter **407**, 1746 (2012).
37. Y. Liu, M. A. Tanatar, V. G. Kogan, H. Kim, T. A. Lograsso, and R. Prozorov, Phys. Rev. B **87**, 134513 (2013).
38. Y. Liu, M. A. Tanatar, W. E. Straszheim, B. Jensen, K. W. Dennis, R. W. McCallum, V. G. Kogan, R. Prozorov, and T. A. Lograsso, Phys. Rev. B **89**, 134504 (2014).
39. See Supplemental Material at [ ] for details, which include Refs. [49–50].
40. H. Hodovanets, Y. Liu, A. Jesche, S. Ran, E. D. Mun, T. A. Lograsso, S. L. Bud'ko, and Paul C. Canfield, Phys. Rev. B **89**, 224517 (2014).
41. C. P. Bean and J. D. Livingston, Phys. Rev. Lett. **12**, 14 (1964).
42. M. Konczykowski, L. I. Burlachkov, Y. Yeshurun, and F. Holtzberg, Phys. Rev. B **43**, 13707 (1991).
43. R. Lortz, N. Musolino, Y. Wang, A. Junod, and N. Toyota, Phys. Rev. B **75**, 094503 (2007).
44. A. B. Pippard, Philos. Mag. **19**, 217 (1969).
45. C. P. Bean, Rev. Mod. Phys. **36**, 31 (1964).
46. D. Dew-Hughes, Philos. Mag. **30**, 293 (1974).
47. E. J. Kramer, J. Appl. Phys. **44**, 1360 (1973).
48. A. M. Campbell and J. E. Evetts, Adv. Phys. **21**, 199 (1972).
49. M. Rotter, M. Pangerl, M. Tegel, and D. Johrendt, Angew. Chem. Int. Ed. **47**, 7949 (2008).
50. S. Avci, O. Chmaissem, D. Y. Chung, S. Rosenkranz, E. A. Goremychkin, J. P. Castellan, I. S. Todorov, J. A. Schlueter, H. Claus, A. Daoud-Aladine, D. D. Khalyavin, M. G. Kanatzidis, and R. Osborn, Phys. Rev. B **85**, 184507 (2012).

51. M. A. Tanatar, A. Kreyssig, S. Nandi, N. Ni, S. L. Bud'ko, P. C. Canfield, A. I. Goldman, and R. Prozorov, Phys. Rev. B **79**, 180508(R) (2009).
52. E. C. Blomberg, M. A. Tanatar, R. M. Fernandes, I. I. Mazin, B. Shen, H.-H. Wen, M. D. Johannes, J. Schmalian, and R. Prozorov, Nat. Commun. **4**, 1914 (2013).
53. Y. Liu, M. A. Tanatar, E. Timmons, and T. A. Lograsso, Crystals **6**, 142 (2016).
54. C. Ma, H. X. Yang, H. F. Tian, H. L Shi, J. B. Lu, Z. W. Wang, L. J. Zeng, G. F. Chen, N. L. Wang, and J. Q. Li, Phys. Rev. B **79**, 060506(R) (2009).
55. C. Tarantini, S. Lee, F. Kametani, J. Jiang, J. D. Weiss, J. Jaroszynski, C. M. Folkman, E. E. Hellstrom, C. B. Eom, and D. C. Larbalestier, Phys. Rev. B **86**, 214504 (2012).
56. Y. Yeshurun, A. P. Malozemoff, and A. Shaulov, Rev. Mod. Phys. **68**, 911 (1996).
57. Y. Abulafia, A. Shaulov, Y. Wolfus, R. Prozorov, L. Burlachkov, Y. Yeshurun, D. Majer, E. Zeldov, H. Wühl, V. B. Geshkenbein, and V. M. Vinokur, Phys. Rev. Lett. **77**, 1596 (1996).
58. D. Giller, A. Shaulov, R. Prozorov, Y. Abulafia, Y. Wolfus, L. Burlachkov, Y. Yeshurun, E. Zeldov, V. M. Vinokur, J. L. Peng, and R. L. Greene, Phys. Rev. Lett. **79**, 2542 (1997).
59. S. Salem-Sugui, Jr., L. Ghivelder, A. D. Alvarenga, L. F. Cohen, H. Luo, and X. Lu, Phys. Rev. B **84**, 052510 (2011).
60. S. Sundar, S. Salem-Sugui, Jr., H. S. Amorim, H.-H. Wen, K. A. Yates, L. F. Cohen, and L. Ghivelder, Phys. Rev. B **95**, 134509 (2017).
61. G. Blatter, M. V. Feigel'man, V. B. Geshkenbein, A. I. Larkin, and V. M. Vinokur, Rev. Mod. Phys. **66**, 1125 (1994).
62. M. V. Feigel'man, V. B. Geshkenbein, and V. M. Vinokur, Phys. Rev. B **43**, 6263(R) (1991).
63. M. V. Feigel'man, V. B. Geshkenbein, A. I. Larkin, and V. M. Vinokur, Phys. Rev. Lett. **63**, 2303 (1989).
64. A. P. Malozemoff and M. P. A. Fisher, Phys. Rev. B **42**, 6784(R) (1990).
65. D. S. Fisher, M. P. A. Fisher, and D. A. Huse, Phys. Rev. B **43**, 130 (1991).

66. V. M. Vinokur, M. V. Feigel'man, and V. B. Geshkenbein, Phys. Rev. Lett. **67**, 915 (1991).

67. M. P. Maley, J. O. Willis, H. Lessure, and M. E. McHenry. Phys. Rev. B **42**, 2639(R) (1990).

68. M. Konczykowski, C. J. van der Beek, M. A. Tanatar, H. Luo, Z. Wang, B. Shen, H. H. Wen, and R. Prozorov, Phys. Rev. B **86**, 024515 (2012).

69. B. Shen, H. Yang, B. Zeng, C. Ren, X. Xu, H.-H. Wen, arXiv:1111.6105 (unpublished).

70. S. Kokkaliaris, P. A. J. de Groot, S. N. Gordeev, A. A. Zhukov, R. Gagnon, and L. Taillefer, Phys. Rev. Lett. **82**, 5116 (1999).

71. S. Kokkaliaris, A. A. Zhukov, P. A. J. de Groot, R. Gagnon, L. Taillefer, and T. Wolf, Phys. Rev. B **61**, 3655 (2000).

72. D. Giller, A. Shaulov, Y. Yeshurun, and J. Giapintzakis, Phys. Rev. B **60**, 106 (1999).

73. S. Salem-Sugui, Jr., L. Ghivelder, A. D. Alvarenga, J. L. Pimentel, Jr., H. Luo, Z. Wang, and H.-H. Wen, Phys. Rev. B **80**, 014518 (2009).

74. M. S. Li, Physics Reports **376**, 133 (2003).

75. A. K. Geim, S. V. Dubonos, J. G. S. Lok, M. Henini, J. C. Maan, Nature **396**, 144 (1998).

76. A. E. Koshelev and A. I. Larkin, Phys. Rev. B **52**, 13559 (1995).

77. V. V. Moshchalkov, X. G. Qiu, and V. Bruyndoncx, Phys. Rev. B **55**, 11793 (1997).

78. S. Riedling, G. Bräuchle, R. Lucht, K. Röhberg, H. v. Löhneysen, H. Claus, A. Erb, and G. Müller-Vogt, Phys. Rev. B **49**, 13283(R) (1994).

79. R. Lucht, H. v. Löhneysen, H. Claus, M. Kläser, and G. Müller-Vogt, Phys. Rev. B **52**, 9724 (1995).

80. A. A. Zhukov, A. V. Volkozub, and P. A. J. de Groot, Phys. Rev. B **52**, 13013 (1995).

81. A. I. Rykov, S. Tajima, and F. V. Kusmartsev, Phys. Rev. B **55**, 8557 (1997).

82. I. Felner, M. I. Tsindlekht, G. Drachuck, and A. Keren, J. Phys.: Condens. Matter. **25**, 065702 (2013).

83. W. A. C. Passos, P. N. Lisboa-Filho, R. Caparroz, C. C. de Faria, P. C. Venturini, F. M.

Araujo-Moreira, S. Sergeenkov, and W. A. Ortiz, Physica C **354**, 189 (2001).

84. J. T. Park, D. S. Inosov, Ch. Niedermayer, G. L. Sun, D. Haug, N. B. Christensen, R. Dinnebier, A. V. Boris, A. J. Drew, L. Schulz, T. Shapoval, U. Wolff, V. Neu, X. Yang, C. T. Lin, B. Keimer, and V. Hinkov, Phys. Rev. Lett. **102**, 117006 (2009).
85. B. P. P. Mallett, C. N. Wang, P. Marsik, E. Sheveleva, M. Yazdi-Rizi, J. L. Tallon, P. Adelmann, Th. Wolf, and C. Bernhard, Phys. Rev. B **95**, 054512 (2017).
86. P. Marsik, K. W. Kim, A. Dubroka, M. Rössle, V. K. Malik, L. Schulz, C. N. Wang, Ch. Niedermayer, A. J. Drew, M. Willis, T. Wolf, and C. Bernhard, Phys. Rev. Lett. **105**, 057001 (2010).
87. W. K. Yeoh, B. Gault, X. Y. Cui, C. Zhu, M. P. Moody, L. Li, R. K. Zheng, W. X Li, X. L. Wang, S. X. Dou, G. L. Sun, C. T. Lin, and S. P. Ringer, Phys. Rev. Lett. **106**, 247002 (2011).
88. A. Iyo, K. Kawashima, T. Kinjo, T. Nishio, S. Ishida, H. Fujihisa, Y. Gotoh, K. Kihou, H. Eisaki, and Y. Yoshida, J. Am. Chem. Soc. **138**, 3410 (2016).

Figure captions

FIG. 1. (Color online) Superconducting transition curves and typical magnetization hysteresis loops (MHLs) of $(Ba_{1-x}K_x)Fe_2As_2$ single crystals (a) x=0.24, (b) x=0.38, (c) x=0.43, (d) x=0.51, (e) x=0.70 at a reduced temperature T/T_c~0.9, and (f) x=0.91 at T/T_c~0.75.

FIG. 2. (Color online) Log-log plots of field dependence of critical current density J_c calculated by the Bean model for the samples (a) x=0.18, (b) x=0.24, (c) x=0.28, (d) x=0.32, (e) x=0.38, (f) x=0.43, (g) x=0.46, (h) x=0.51, (i) x=0.64, (j) x=0.70, (k) x=0.77, and (l) x=0.91. Red dashed lines indicate a power law dependence of J_c.

FIG. 3. (Color online) The normalized pinning force density F_p/F_p^{max} against the reduced field $h = H/H_{irr}$ for the (a) x=0.18, (b) x=0.24, (c) x=0.38, (d) x=0.43, (e) x=0. 46, (f) x=0.51, (g) x=0.64, and (h) x=0.70. The arrows indicate the peak position.

FIG. 4. (Color online) (a) The critical current density J_c are extracted at H=0.5 T and plotted as a function of the reduced temperature T/T_c for $(Ba_{1-x}K_x)Fe_2As_2$ crystals. (b) J_c values are further extracted at the different reduced temperatures T/T_c=0.20, 0.52, and 0.80. The doping dependence of J_c is plotted, which illustrates that J_c reaches maximum at around x=0.26. The arrow indicates a local minimum at x=0.46.

FIG. 5. (Color online) (a) Dislocations observed in the sample x=0.38. (b) A needle-like inclusion is observed along [100] zone axis, indicated in the red frame. (c) Higher magnification image of the needle-like inclusion. (d) Coherent growth of crystal lattice at the end of needle-like

inclusion. HR-STEM images taken along (e) [001] and (f) [100] zone axis, respectively, for the sample x=0.38. HR-STEM image along [100] zone axis reveals the undulation of the FeAs layers in the sample.

FIG. 6. (Color online) (a) Dislocations in the sample x=0.46. (b) A needle-like inclusion is found in the cross section obtained by using FIB for the sample x=0.46. The length is ~30 nm. (c) HR-STEM image along [100] zone axis displays the undulation of the FeAs layers in the sample x=0.46. (d) Selected area electron diffraction (SAED) pattern of the sample x=0.46 along [100] zone axis. (e) HR-STEM image along [100] zone axis for the sample x=0.65. (f) The needle-like inclusion is also found in the sample x=0.65.

FIG. 7. (Color online) (a)-(b) Double-logarithmic plots of time dependence of magnetization at different fields at T=20 K for the sample x=0.24. The red dashed lines indicate the power law dependence. (c) The MHL at T=20 K shows a SMP at H_{sp}=2.7 T. The empty circles represent the magnetization decay data during a period of 1×10^4 seconds. It can be seen that the SMP shifts to $H'_{sp} = 2$ T, indicated by an arrow. The relaxation rate S shows a minimum at S_{min}=1.5 T. Blue solid line is guide to the eye. (d) The plots of $-T\ln|dM/dt|$ vs $|M|$, which equals an activation energy U vs J relation. The slope of activation energy U changes at the $H'_{sp} = 2$, which signifies a crossover from elastic to plastic creep.

FIG. 8. (Color online) (a) The decay of magnetization at different temperatures at H=0.5 T for the sample x=0.24. (b) The temperature dependence of relaxation rate S at a fixed field H=0.5 T shows a broad peak at around T=10 K. Solid line is guide to the eye. (c) Semi-logarithmic plot of

the current density dependence of the activation energy U at H=0.5 T. The solid line corresponds to the linear fitting with Eq. (5).

FIG. 9. (Color online) The MHLs together with magnetic relaxation data at (a) T=20 K and (b) T=33 K for the sample x=0.32. The relaxation rate S shows a kink where the MHL has an onset peak. (c) The temperature dependence of relaxation rate S at a fixed field H=0.5 T shows a broad peak at around T=14 K. (d) The current density dependent U at H=0.5 T fitted by Eq. (5).

FIG. 10. (Color online) Double-logarithmic plots of the time dependence of magnetization (a) at different temperatures at H=0.5 T and (b) at different fields at T=20 K for the sample x=0.43. (c) The MHL together with magnetic relaxation data at T=20 K. (d) The temperature dependence of relaxation rate S at H=0.5 T, which rapidly increases above T=20 K. (l) The current density dependent U at H=0.5 T fitted by Eq. (5).

FIG. 11. (Color online) Double-logarithmic plots of the time dependence of magnetization (a) at different fields at T=19 K and (b) at different temperatures at H=0.5 T for the sample x=0.62. (c) The MHL together with magnetic relaxation data at T=19 K. (d) The temperature dependence of relaxation rate S at H=0.5 T, which rapidly increases above T=16 K. (l) The current density dependent U at H=0.5 T fitted by Eq. (5).

FIG. 12. (Color online) (a) Double-logarithmic plots of the time dependence of magnetization at different temperatures at H=0.5 T for the sample x=0.70. Arrow indicates the time when the magnetization deceases to its equilibrium value. (b) The temperature dependence of relaxation

rate S at H=0.5 T, which rapidly increases above T=5 K. (l) The current density dependent U at H=0.5 T fitted by Eq. (5).

FIG. 13. (Color online) (a) The normalized temperature T/T_c dependence of relaxation rate S for the $(Ba_{1-x}K_x)Fe_2As_2$ (x=0.24, 0.32, 0.43, 0.62, and 0.70) single crystals. (b) The doping dependence of relaxation data S at three reduced temperatures T/T_c=0.2, 0.4 and 0.6 (left axis) and of activation barrier U_0 (right axis). The values of relaxation rate S at different reduced temperatures were obtained by interpolation from the curves shown in (a).

FIG. 14. (Color online) Temperature dependence of magnetization measured in both ZFC and FC procedures for $(Ba_{1-x}K_x)Fe_2As_2$ single crystals; (a) x=0.24, (b) x=0.32, (c) x=0.43, and (d) x=0.64. The arrows indicate the increase of applied magnetic fields. The insets in the Figures show the transition curves in the vicinity of T_c. A dip below T_c, i.e. the PME, is clearly observed in the samples x=0.24, 0.32, and 0.64.

FIG. 15. Temperature dependence of magnetization for $(Ba_{1-x}K_x)Fe_2As_2$ (x=0.32) single crystals at H=7 T in the configuration $H \parallel c$. The data were collected on warming process. The samples were cooled down to 3 K at different cooling rate: 10, 5, 2, and 1 K/min. The inset shows the transition curves in the vicinity of T_c. The jump due to PME effect is gradually weakened with decreasing cooling rate.

TABLE I. Critical transition temperature T_c(onset) of $(Ba_{1-x}K_x)Fe_2As_2$ single crystals and transition width ΔT_c. T_c(onset) is defined as the temperature where susceptibility data $\chi(T)$ show a diamagnetic drop, while ΔT_c corresponds to the temperature difference where $\chi(T)$ drops from 10% to 90%.

K content x	0.18	0.22	0.24	0.26	0.28	0.32	0.38	0.43
T_c (onset) (K)	11.5	22.6	26.6	31.1	34.6	37.5	38.6	38.4
ΔT_c (K)	1.6	1.2	0.5	0.5	0.5	0.4	0.4	0.6

(Continued)

0.46	0.51	0.62	0.64	0.70	0.77	0.91	1
37.9	34.0	25.8	23.8	18.3	15.8	7.3	3.5
0.8	0.8	0.9	1.4	1.1	3	0.7	0.5

TABLE II. The current density J (presented by the magnetization) dependence of the activation energy U for $(Ba_{1-x}K_x)Fe_2As_2$ (x=0.24, 0.32, 0.43, 0.62 and 0.70) single crystals is fitted by Eq. (5): $U(J) = U_0 \ln(J_c/J)$. The fitting parameters are summarized in this Table.

K content x	C	U_0	J_c
0.24	40	277.1	7978.8
0.32	40	300.7	13829.4
0.43	36	194.3	6379.3
0.62	8	181.8	136.4
0.70	8	25.5	128.5

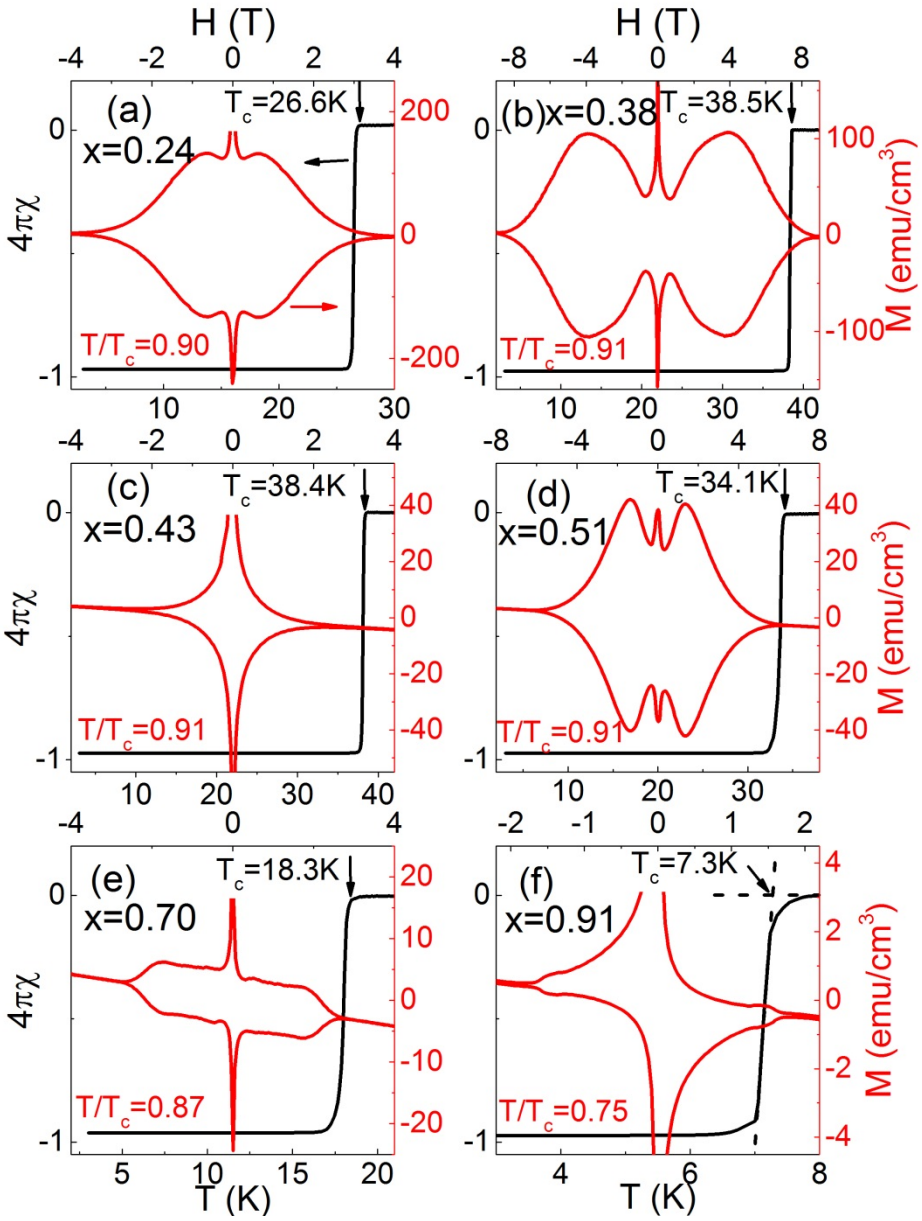
H (T)
H (T)
(a)
x=0.24
T_c=26.6K
T/T_c=0.90
(b)x=0.38
T_c=38.5K
T/T_c=0.91
(c)
x=0.43
T_c=38.4K
T/T_c=0.91
(d)
x=0.51
T_c=34.1K
T/T_c=0.91
(e)
x=0.70
T_c=18.3K
T/T_c=0.87
(f)
x=0.91
T_c=7.3K
T/T_c=0.75
4πχ
M (emu/cm^3)
T (K)
T (K)

Figure 1

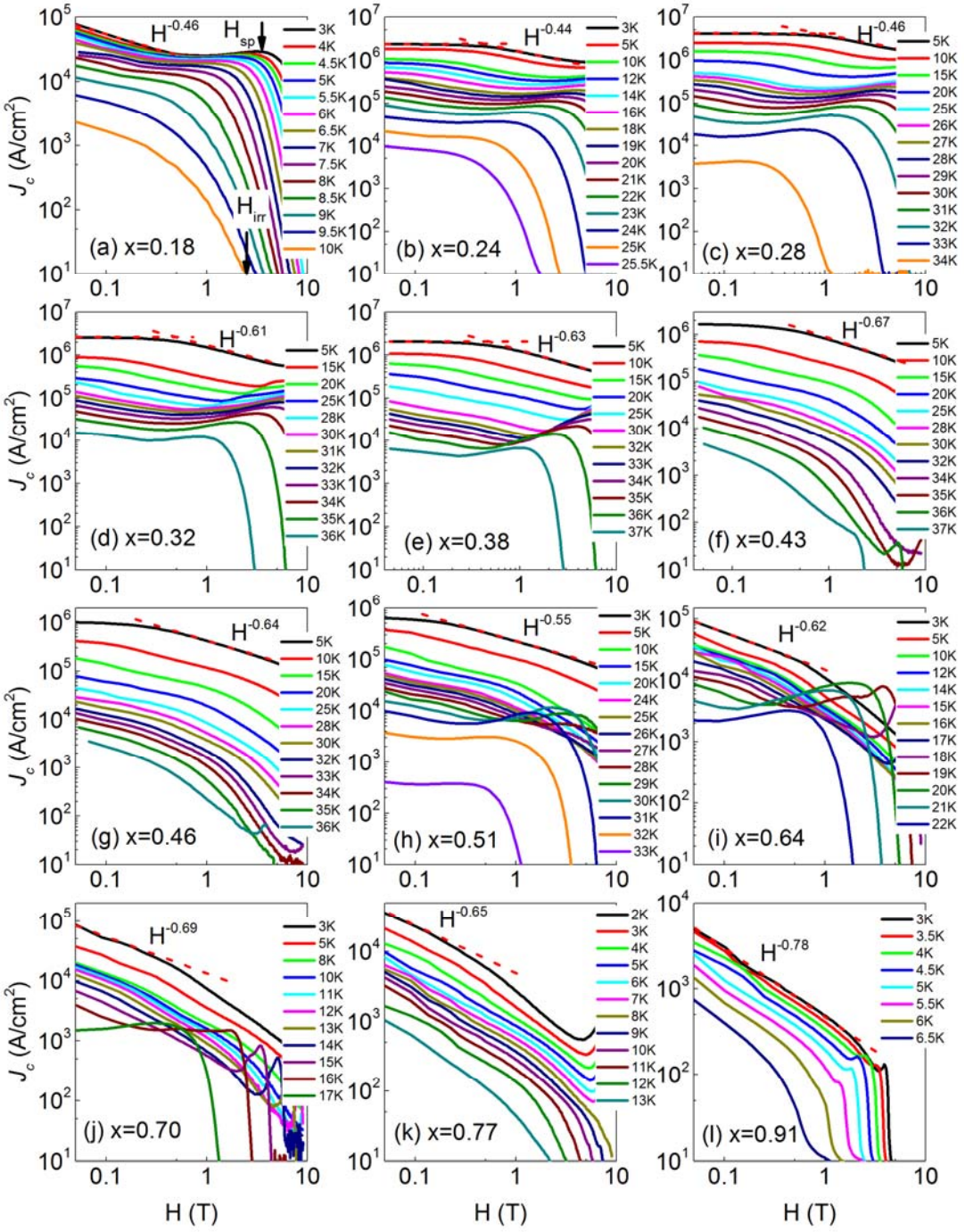
(a) x=0.18
(b) x=0.24
(c) x=0.28
(d) x=0.32
(e) x=0.38
(f) x=0.43
(g) x=0.46
(h) x=0.51
(i) x=0.64
(j) x=0.70
(k) x=0.77
(l) x=0.91
H^-0.46
H_sp
H_irr
H^-0.44
H^-0.46
H^-0.61
H^-0.63
H^-0.67
H^-0.64
H^-0.55
H^-0.62
H^-0.69
H^-0.65
H^-0.78
J_c (A/cm^2)
H (T)

Figure 2

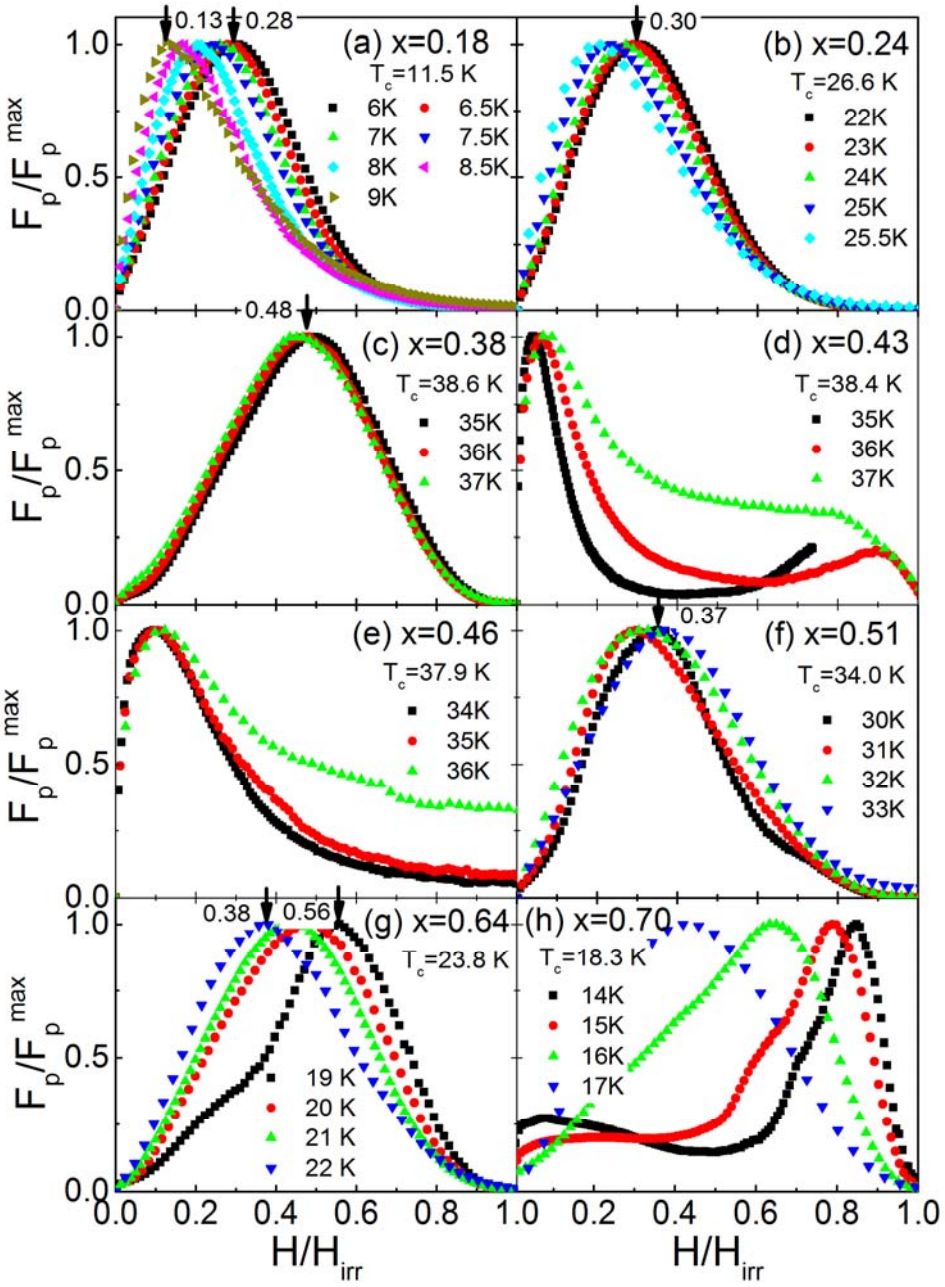
0.13
0.28
(a) x=0.18
T_c=11.5 K
6K
6.5K
7K
7.5K
8K
8.5K
9K
0.30
(b) x=0.24
T_c=26.6 K
22K
23K
24K
25K
25.5K
0.48
(c) x=0.38
T_c=38.6 K
35K
36K
37K
(d) x=0.43
T_c=38.4 K
35K
36K
37K
0.37
(e) x=0.46
T_c=37.9 K
34K
35K
36K
(f) x=0.51
T_c=34.0 K
30K
31K
32K
33K
0.38
0.56
(g) x=0.64
T_c=23.8 K
19 K
20 K
21 K
22 K
(h) x=0.70
T_c=18.3 K
14K
15K
16K
17K
F_p/F_p^max
H/H_irr
0.0
0.2
0.4
0.6
0.8
1.0
0.5

Figure 3

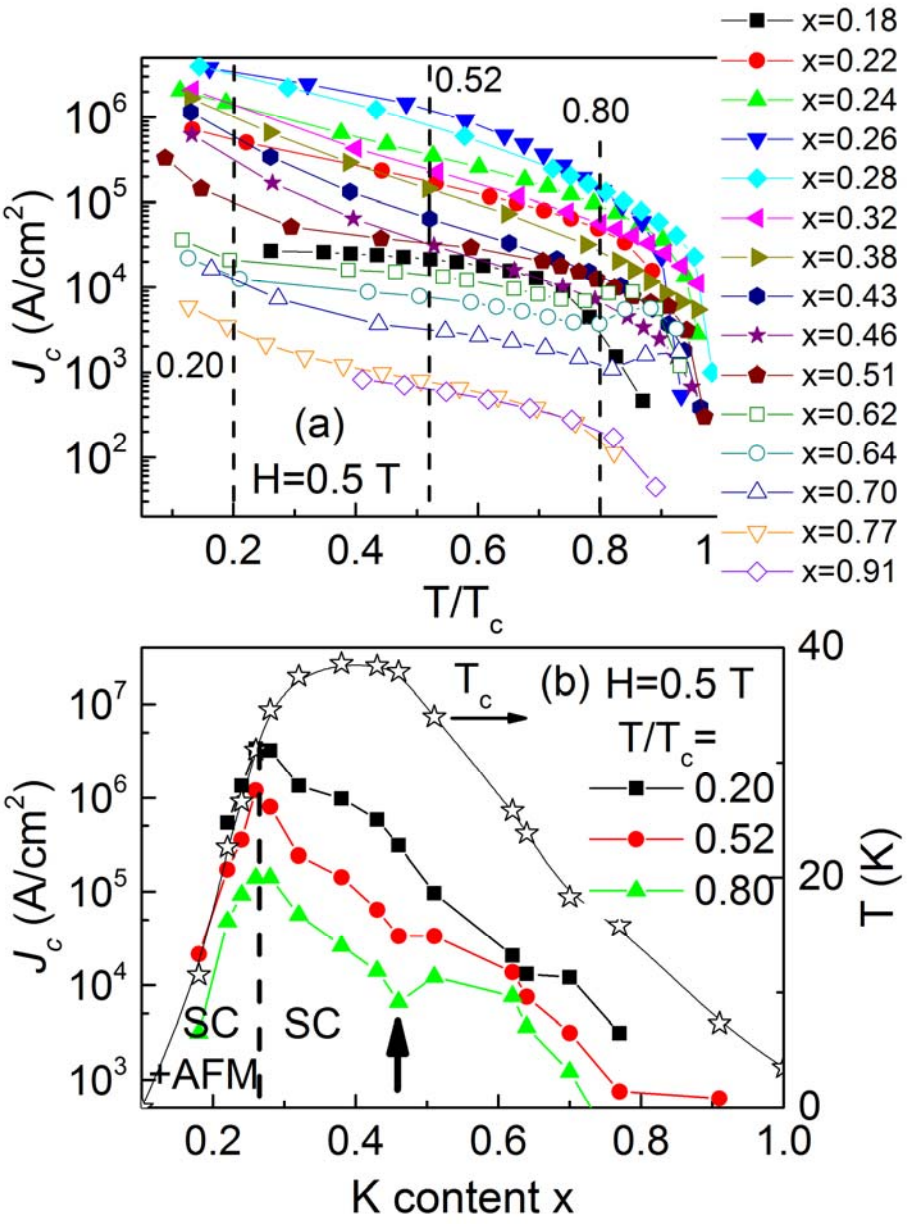
x=0.18
x=0.22
x=0.24
x=0.26
x=0.28
x=0.32
x=0.38
x=0.43
x=0.46
x=0.51
x=0.62
x=0.64
x=0.70
x=0.77
x=0.91
0.52
0.80
0.20
(a)
H=0.5 T
J_c (A/cm^2)
T/T_c
T_c
(b) H=0.5 T
T/T_c =
0.20
0.52
0.80
SC
+AFM
SC
T (K)
K content x

Figure 4

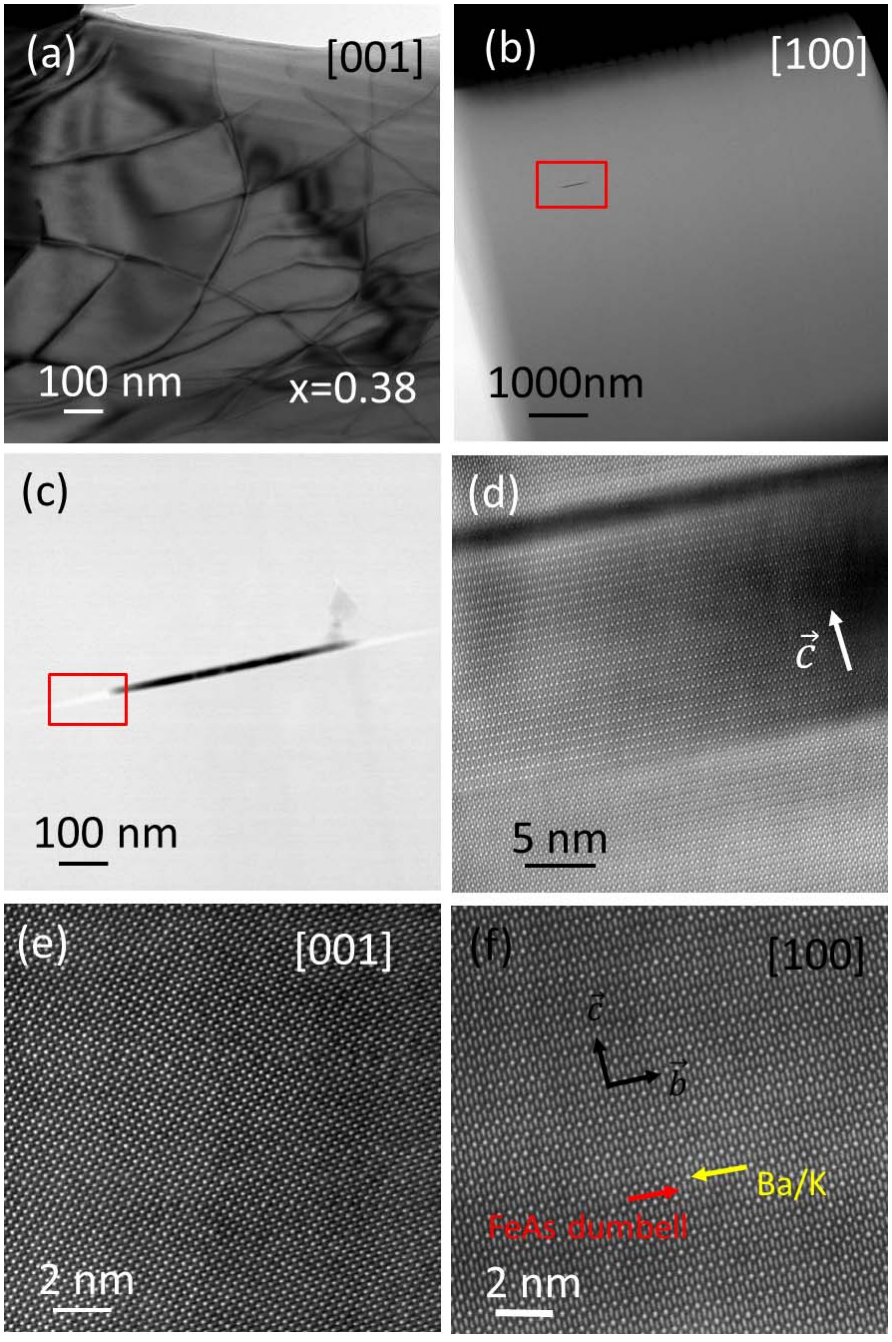
(a)
[001]
100 nm
x=0.38
(b)
[100]
1000nm
(c)
100 nm
(d)
$\vec{c}$
5 nm
(e)
[001]
2 nm
(f)
[100]
$\vec{c}$
$\vec{b}$
Ba/K
FeAs dumbell
2 nm

Figure 5

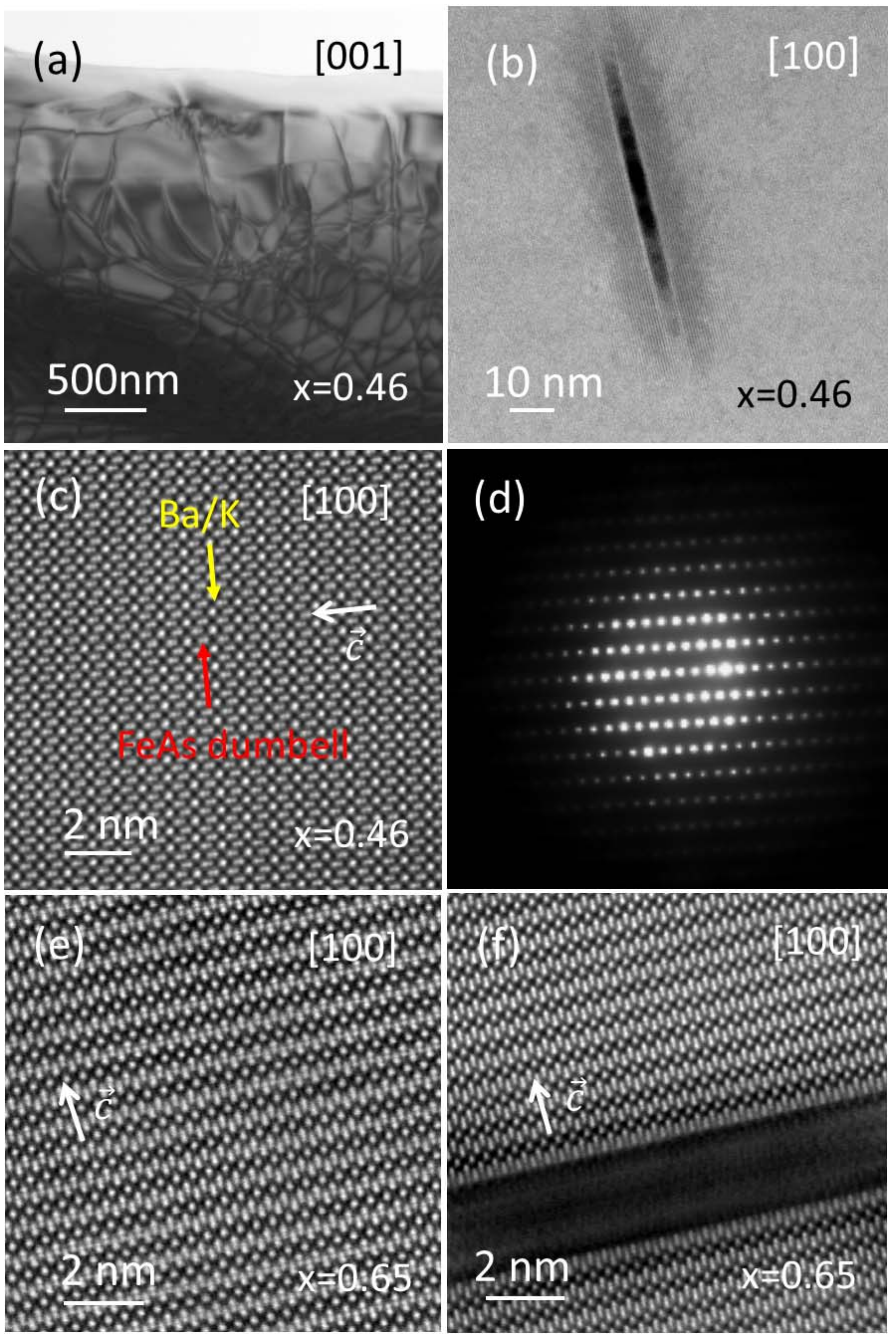
(a)
[001]
500nm
x=0.46
(b)
[100]
10 nm
x=0.46
(c)
Ba/K
[100]
$\vec{c}$
FeAs dumbell
2 nm
x=0.46
(d)
(e)
[100]
$\vec{c}$
2 nm
x=0.65
(f)
[100]
$\vec{c}$
2 nm
x=0.65

Figure 6

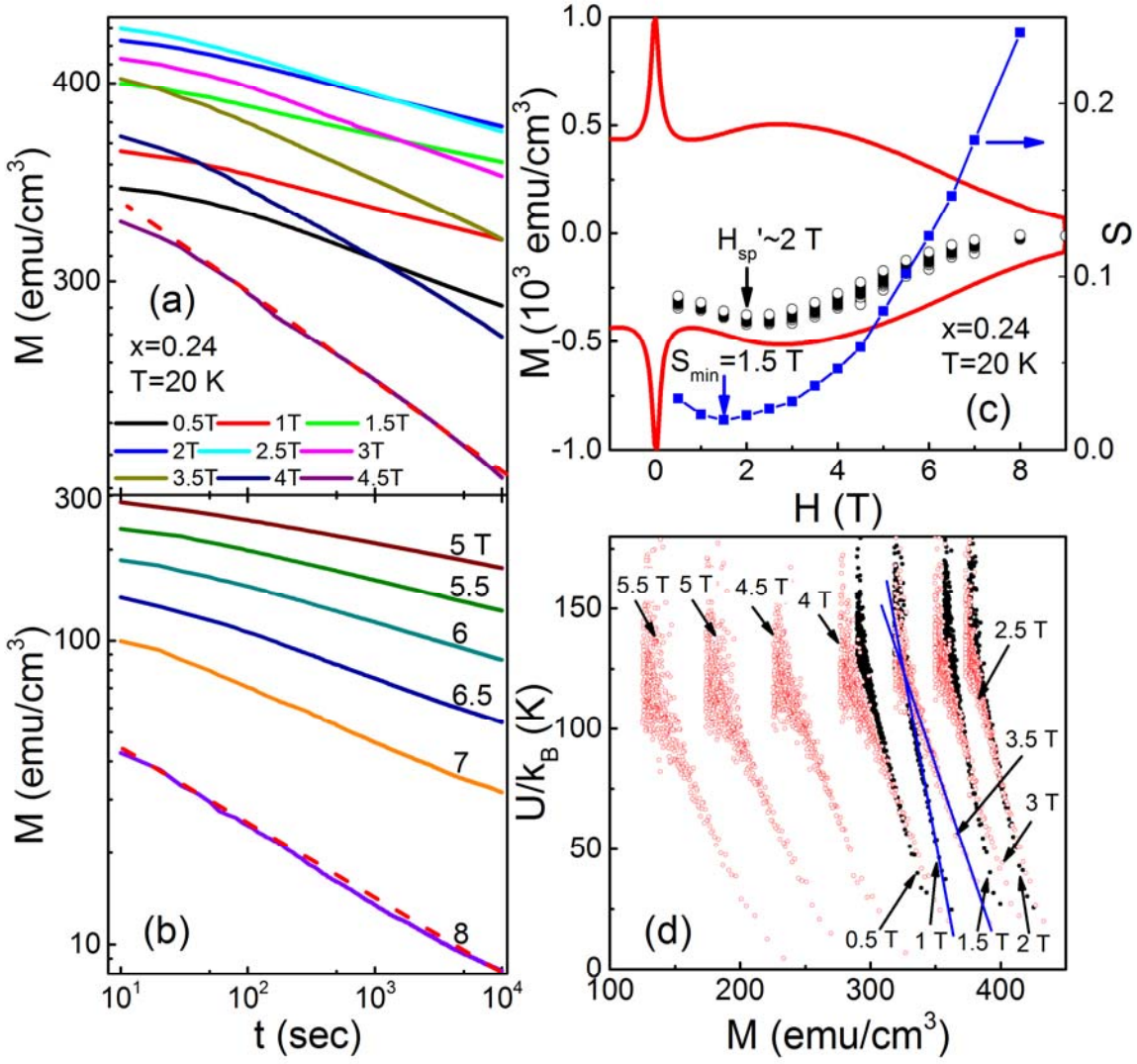
(a)
x=0.24
T=20 K
0.5T 1T 1.5T
2T 2.5T 3T
3.5T 4T 4.5T
M (emu/cm3)
(b)
5 T
5.5
6
6.5
7
8
t (sec)
(c)
Hsp'~2 T
Smin=1.5 T
x=0.24
T=20 K
M (10^3 emu/cm^3)
S
H (T)
(d)
5.5 T 5 T 4.5 T 4 T
2.5 T
3.5 T
3 T
0.5 T 1 T 1.5 T 2 T
U/kB (K)
M (emu/cm3)

Figure 7

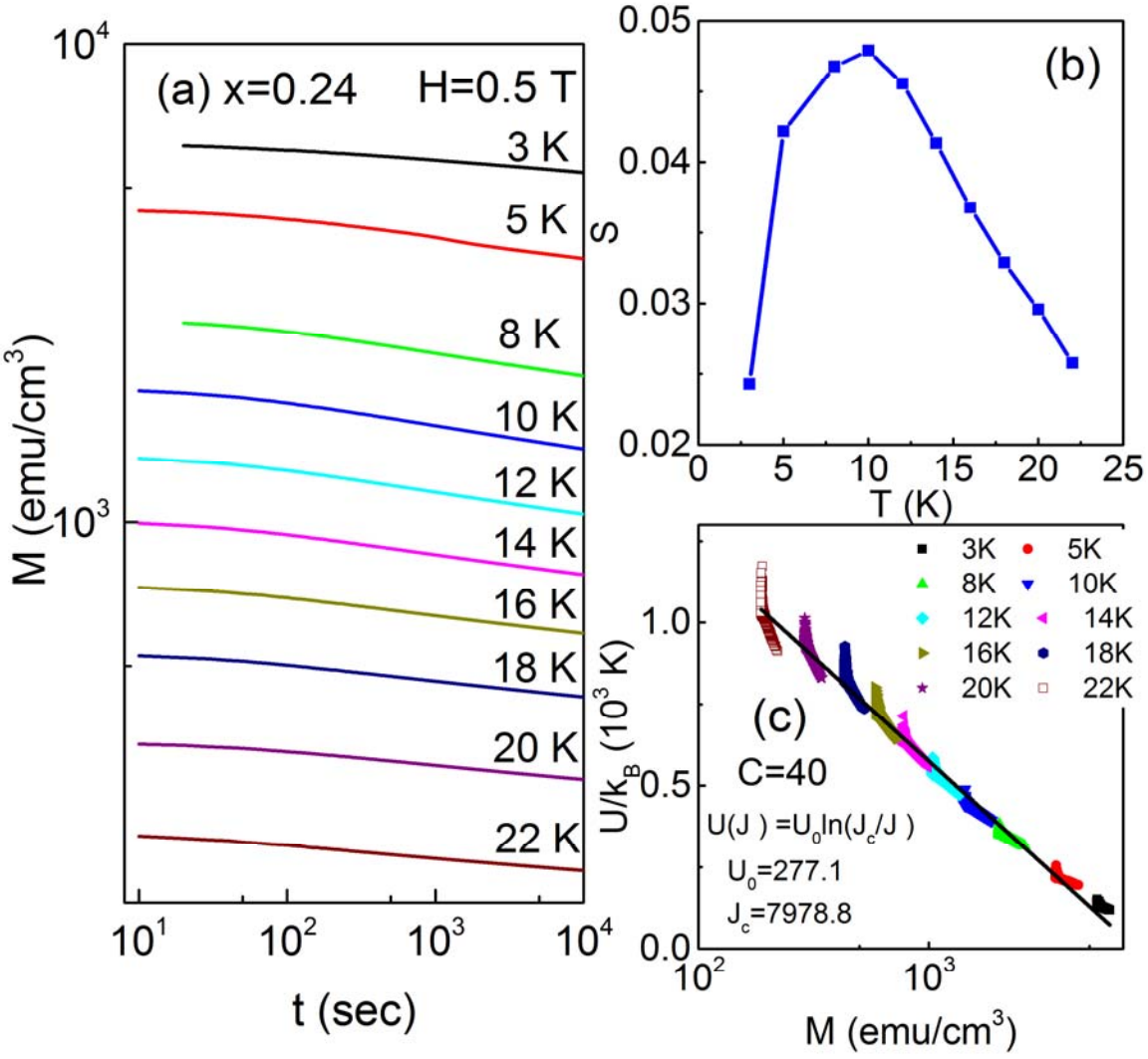
(a) x=0.24 H=0.5 T
3 K
5 K
8 K
10 K
12 K
14 K
16 K
18 K
20 K
22 K
M (emu/cm3)
t (sec)
(b)
S
T (K)
(c)
3K
5K
8K
10K
12K
14K
16K
18K
20K
22K
C=40
U(J) =U0ln(Jc/J)
U0=277.1
Jc=7978.8
U/kB (10^3 K)
M (emu/cm3)

Figure 8

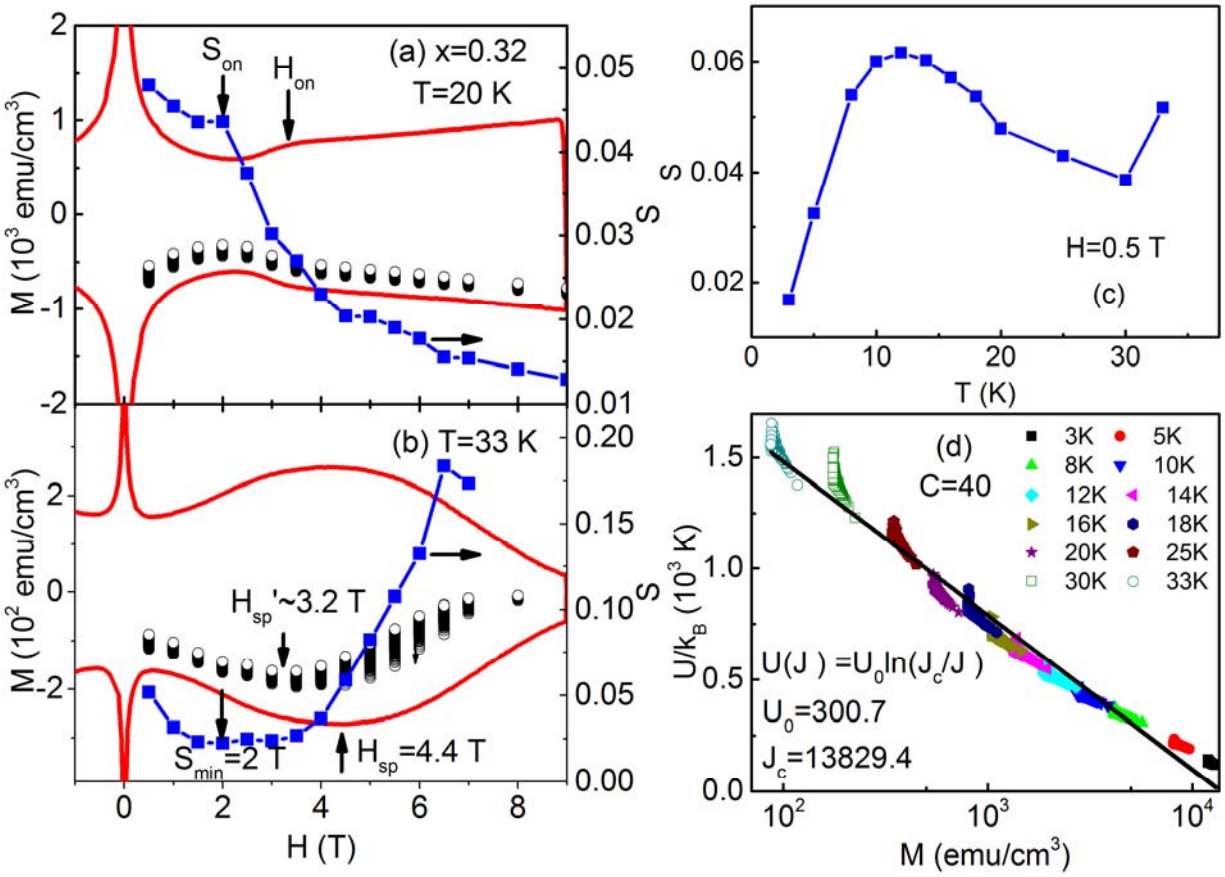
(a) x=0.32
T=20 K
S_on
H_on
M (10^3 emu/cm^3)
S
(b) T=33 K
H_sp'~3.2 T
S_min=2 T
H_sp=4.4 T
M (10^2 emu/cm^3)
H (T)
H=0.5 T
(c)
T (K)
(d)
C=40
3K
5K
8K
10K
12K
14K
16K
18K
20K
25K
30K
33K
U(J) =U_0ln(J_c/J)
U_0=300.7
J_c=13829.4
U/k_B (10^3 K)
M (emu/cm^3)

Figure 9

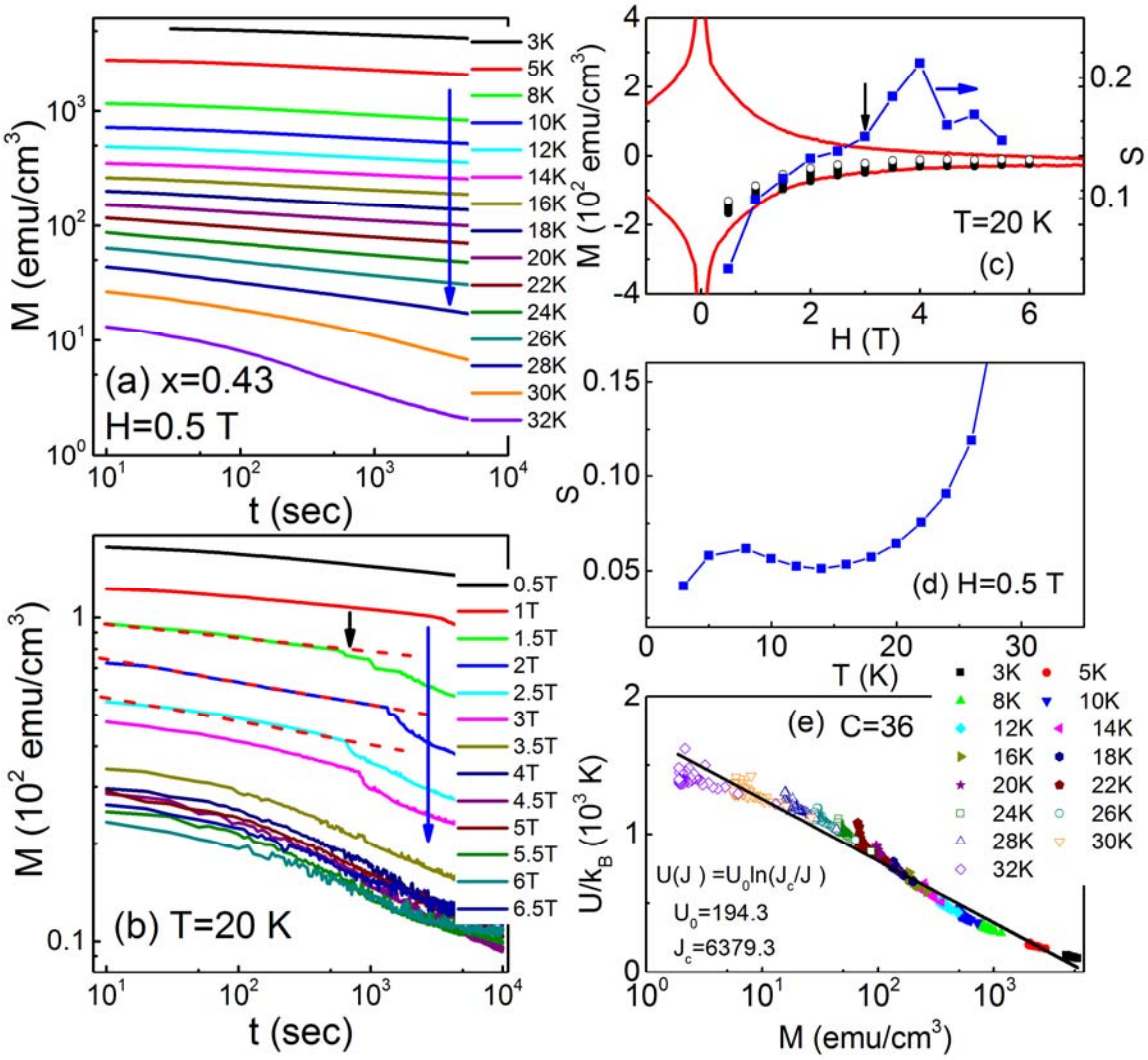
M (emu/cm3)
t (sec)
(a) x=0.43
H=0.5 T
3K
5K
8K
10K
12K
14K
16K
18K
20K
22K
24K
26K
28K
30K
32K
M (10^2 emu/cm^3)
(b) T=20 K
0.5T
1T
1.5T
2T
2.5T
3T
3.5T
4T
4.5T
5T
5.5T
6T
6.5T
M (10^2 emu/cm^3)
H (T)
T=20 K
(c)
S
T (K)
(d) H=0.5 T
U/k_B (10^3 K)
M (emu/cm^3)
(e) C=36
U(J) =U_0ln(J_c/J)
U_0=194.3
J_c=6379.3

Figure 10

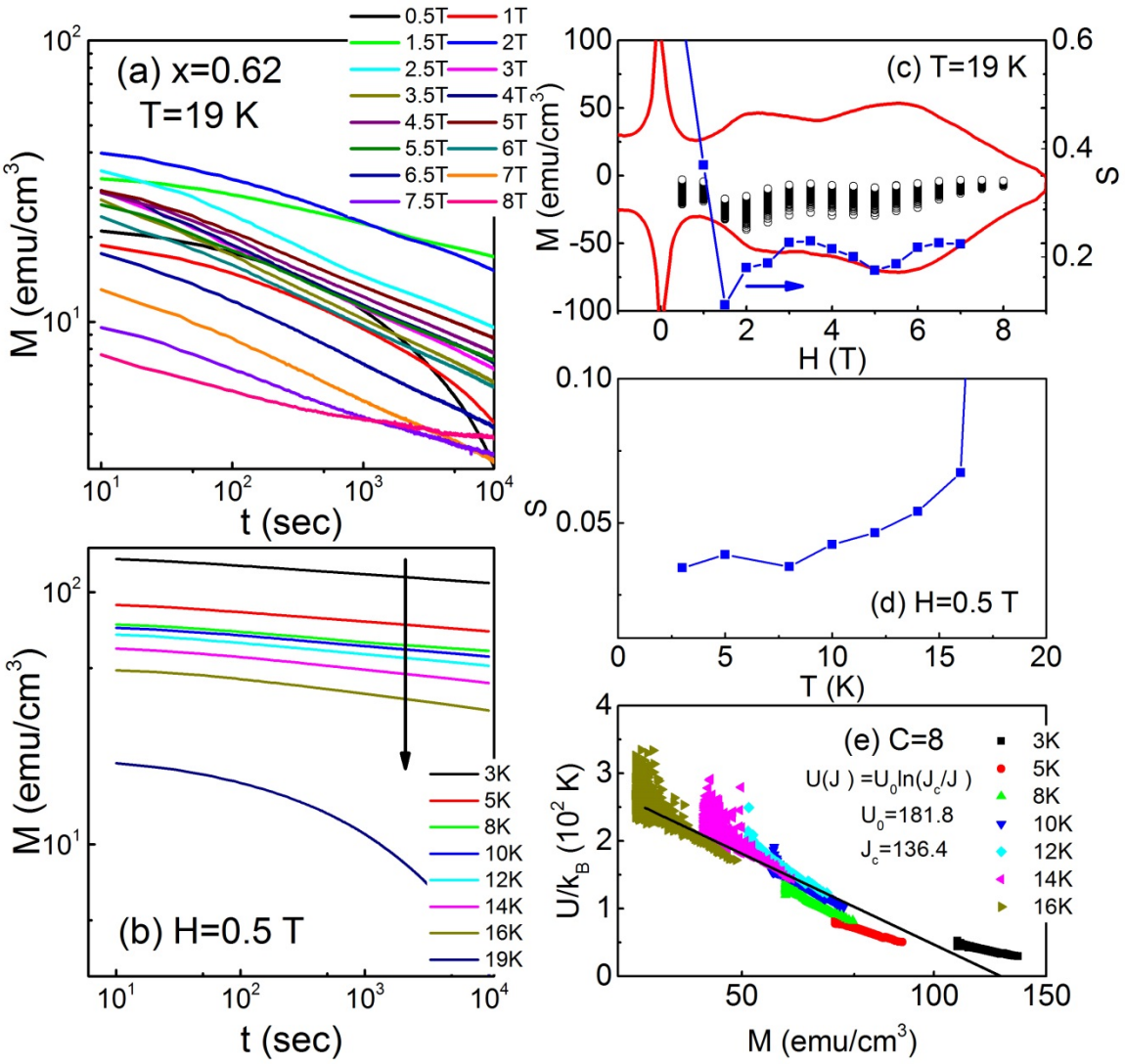
(a) x=0.62
T=19 K
0.5T
1T
1.5T
2T
2.5T
3T
3.5T
4T
4.5T
5T
5.5T
6T
6.5T
7T
7.5T
8T
M (emu/cm3)
t (sec)
(b) H=0.5 T
3K
5K
8K
10K
12K
14K
16K
19K
(c) T=19 K
M (emu/cm3)
S
H (T)
(d) H=0.5 T
T (K)
(e) C=8
U(J) =U0ln(Jc/J)
U0=181.8
Jc=136.4
U/kB (10^2 K)
M (emu/cm3)

Figure 11

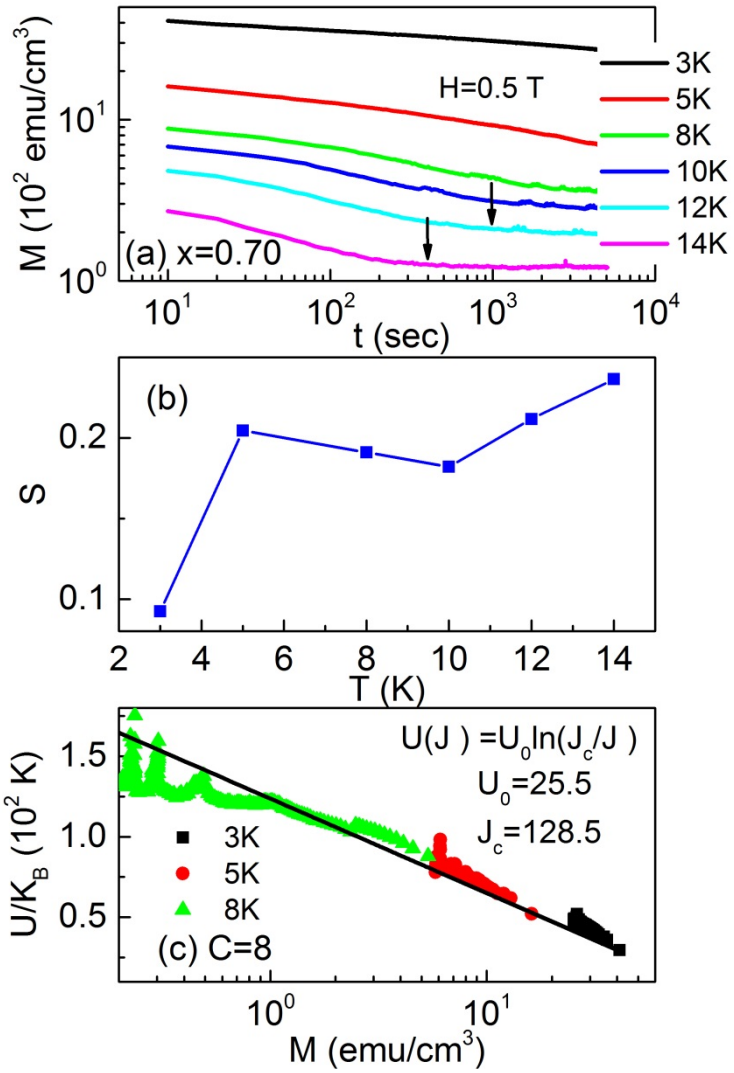
M (10^2 emu/cm^3)
H=0.5 T
3K
5K
8K
10K
12K
14K
(a) x=0.70
t (sec)
(b)
S
T (K)
U/K_B (10^2 K)
U(J) =U_0ln(J_c/J)
U_0=25.5
J_c=128.5
3K
5K
8K
(c) C=8
M (emu/cm^3)

Figure 12

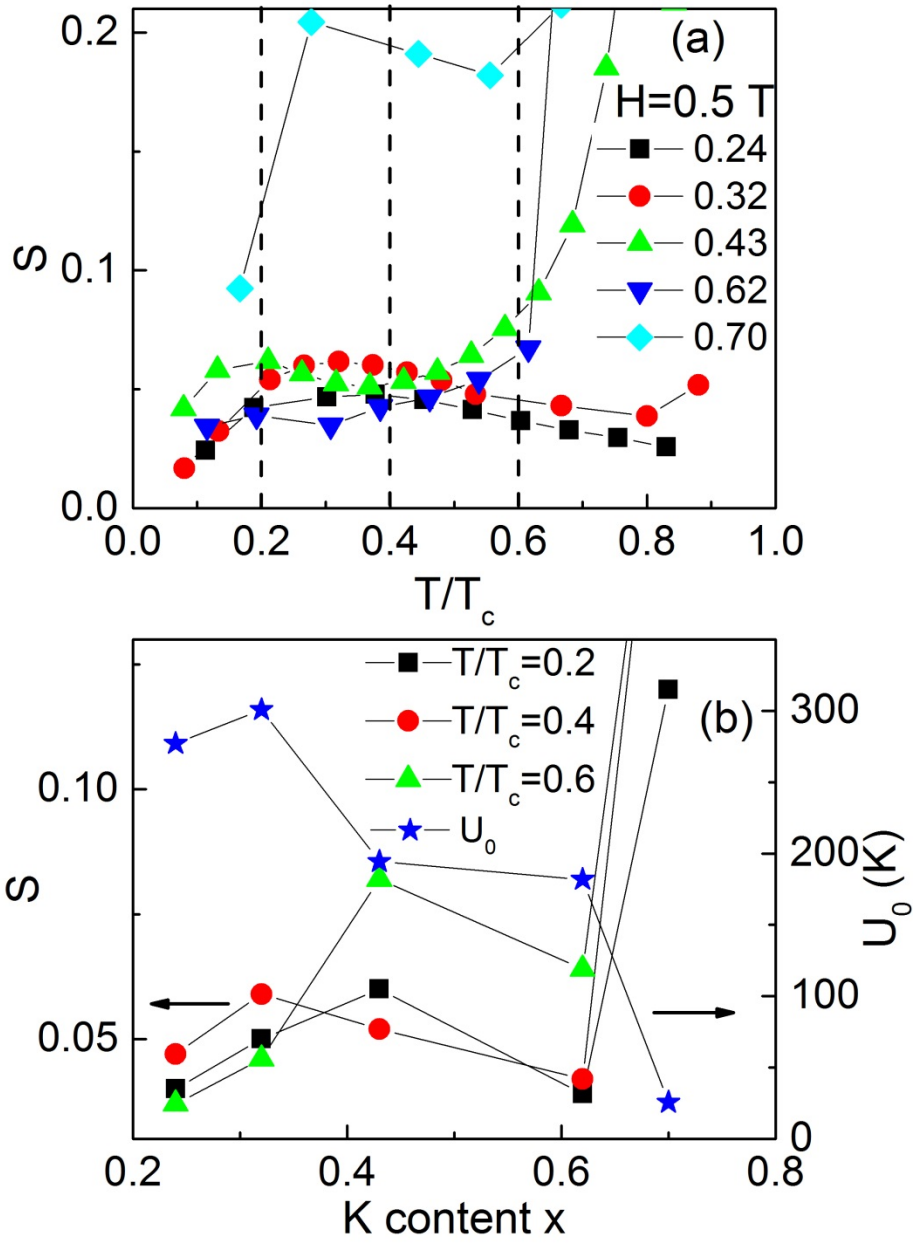
(a)
H=0.5 T
0.24
0.32
0.43
0.62
0.70
S
T/T_c
(b)
T/T_c=0.2
T/T_c=0.4
T/T_c=0.6
U_0
S
U_0 (K)
K content x

Figure 13

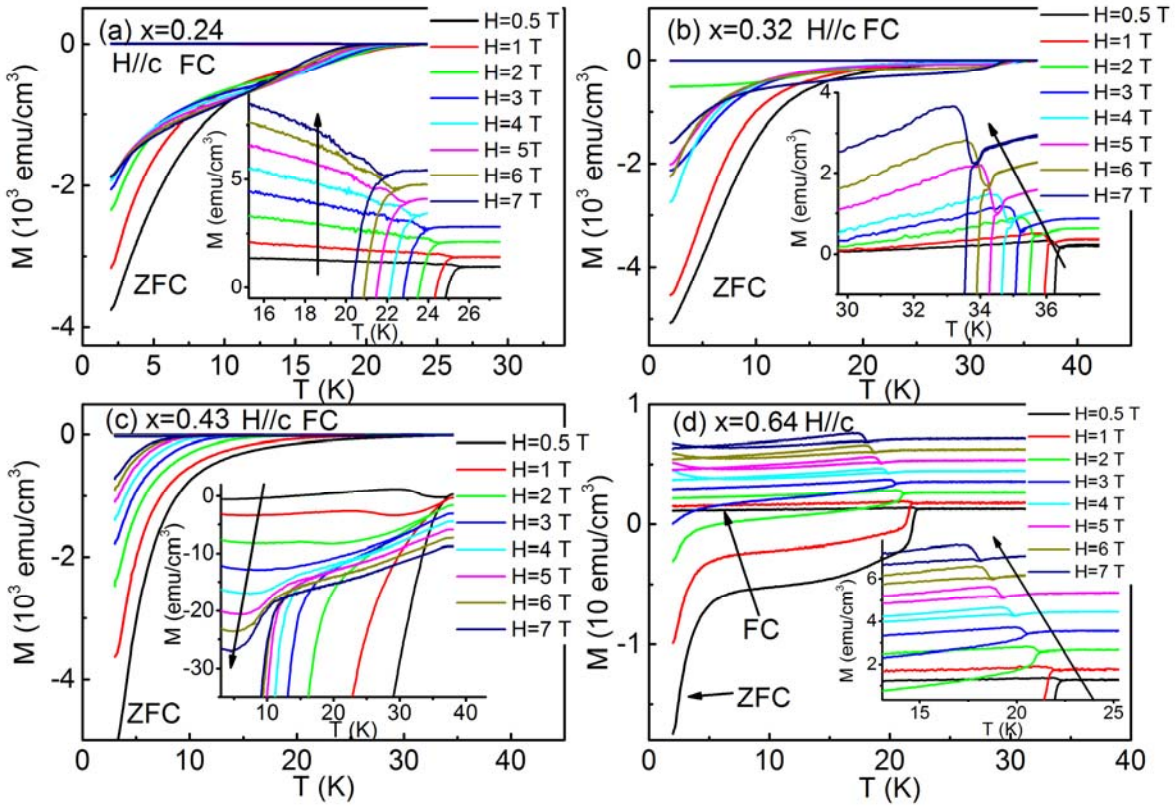
(a) x=0.24
H//c FC
ZFC
H=0.5 T
H=1 T
H=2 T
H=3 T
H=4 T
H= 5T
H=6 T
H=7 T
M (10^3 emu/cm^3)
T (K)
M (emu/cm^3)
T (K)
(b) x=0.32 H//c FC
ZFC
(c) x=0.43 H//c FC
ZFC
(d) x=0.64 H//c
FC
ZFC
M (10 emu/cm^3)

Figure 14

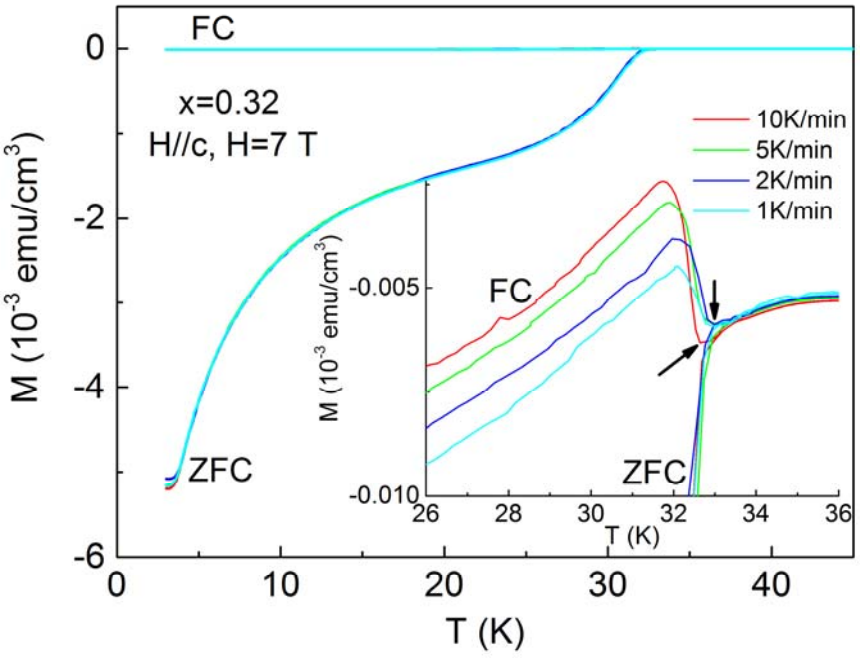
FC
x=0.32
H//c, H=7 T
10K/min
5K/min
2K/min
1K/min
ZFC
M (10^-3 emu/cm^3)
T (K)
0
-2
-4
-6
0
10
20
30
40
-0.005
-0.010
26
28
30
32
34
36

Figure 15